

# Microfabrication of the Ammonia Plasma-Activated Nickel Nitride–Nickel Thin Film for Overall Water Splitting in the Microfluidic Membraneless Electrolyzer

Biswajit S. De, Pawan Kumar, Neeraj Khare, Jing-Li Luo, Anastasia Elias,\* and Suddhasatwa Basu\*

Cite This: <https://doi.org/10.1021/acsaem.1c01772>

Read Online

ACCESS |



Metrics &amp; More



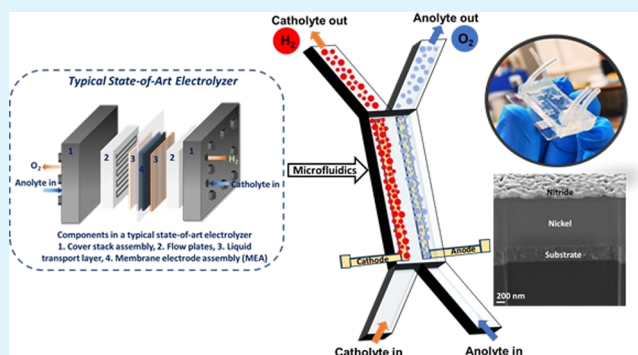
Article Recommendations



Supporting Information

**ABSTRACT:** Hydrogen production in the microfluidic alkaline membraneless electrolyzer ( $\mu$ AME) marks a new paradigm in sustainable energy technology. One challenge in this field is implementing a bifunctional catalyst to catalyze hydrogen evolution reaction and oxygen evolution reaction using methods compatible with microfabrication techniques. Herein, the scalable synthesis, micropatterning, and performance of a nickel nitride ( $\text{Ni}_3\text{N}/\text{Ni}$ ) bifunctional catalyst are demonstrated. Microfabrication is used to pattern Ni microelectrodes, and nitridation and N–H grafting of the electrodes—which also act as the catalysts—are achieved by ammonia plasma. These electrodes are incorporated into the  $\mu$ AME device, and the electrolyte flow rate is optimized to maximize gas product separation. The  $\mu$ AME is operated in a two-electrode configuration exhibiting a current density of  $263.73 \text{ mA cm}^{-2}$  at 2.5 V and a stable 6 h operation for overall water splitting. The  $\mu$ AME performance efficiency is 99.86%, with a current density of  $150 \text{ mA cm}^{-2}$ . Gas chromatography of the electrolysis products revealed no gas cross-over across the electrodes. Volumetric collection efficiencies of 97.72% for  $\text{H}_2$  and 96.14% for  $\text{O}_2$  are obtained. The performance of the  $\mu$ AME is comparable to a membrane-based electrolyzer operating under stringent conditions of high temperature (60–80 °C) and extreme electrolyte pH (30–40 wt % KOH).

**KEYWORDS:** microfluidics, membraneless, microfabrication, overall water splitting, hydrogen energy, bifunctional catalyst



## 1. INTRODUCTION

The global appetite for energy is increasing, and advancements in renewable energy technologies are sorely needed to limit climate change associated with nonrenewable resources. Fuels such as hydrogen ( $\text{H}_2$ ), in which solar energy is stored in chemical bonds, are highly desirable to enable renewable energy storage.<sup>1</sup>  $\text{H}_2$  has an energy density of 140 MJ/kg, which is higher than the energy stored in supercapacitors ( $\sim 0.01 \text{ MJ/kg}$ ), batteries ( $\sim 0.1\text{--}0.5 \text{ MJ/kg}$ ), and liquid fuels ( $\sim 50 \text{ MJ/kg}$ ).<sup>2,3</sup> Water electrolysis can be undertaken in an electrolyzer to produce high purity  $\text{H}_2$  utilizing excess energy from renewable sources.

A typical water electrolyzer (Figure 1) consists of a sandwiched structure. The anode and cathode are stacked on either side of a membrane to form a membrane-electrode assembly (MEA). An ion-selective membrane in the middle of the stack permeates selective ion migration ( $\text{H}^+/\text{OH}^-$ ) and evades  $\text{H}_2$  and  $\text{O}_2$  cross-over across the electrodes. One limiting factor in the design and operation of electrolyzers is that membrane conductivity is typically highest at extreme pH values. A low resistance ionic route through the membrane is achieved using a high acidic media in the cation exchange membrane and a strong alkaline media in the anion exchange

membrane.<sup>4,5</sup> The extreme electrolyte pH accelerates membrane degradation in the electrolyzer, initiating the cross-over of counterions and gas products. Electrolyzers operating in acidic pH require noble metal-based catalysts for stable operation at high current density.<sup>5,6</sup> Transition metal-based catalysts that are abundant can be used in an alkaline electrolyzer but suffer from the low performance of the electrolyzer due to the poor conductivity of the anion exchange membrane.<sup>7–9</sup> Electrolyzers include additional components such as a liquid transport layer and flow plates (Figure 1), whose primary functions are reactants/products transport to and from the reaction sites and electron and heat conduction, with minimum ohmic, activation, fluidic, thermal, and interfacial losses.<sup>10–12</sup>

Received: June 19, 2021

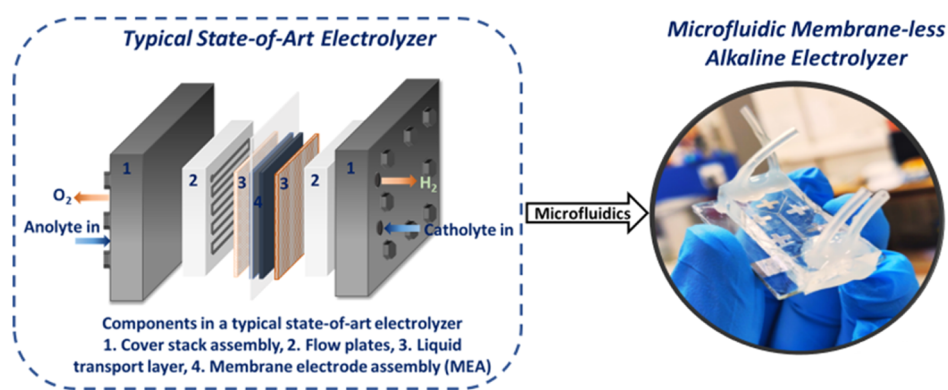


**Figure 1.** Stacked, multilayer structure of a typical state-of-art electrolyzer can be implemented on a single chip using microfluidics.

Microfluidics offers immense benefits for electrochemical energy conversion on a microscale. The challenges in the conventional membrane-based electrolyzers can be resolved by performing microfluidic energy conversion. An enhancement in the intrinsic properties is realized by reducing the characteristic length (length, width, and depth of the microchannel and interelectrode distance) to microscale. A strategic approach using microfluidics minimizes the number of components and condenses the membrane-based electrolyzers to a single chip (Figure 1).

The concentration gradient in the microfluidic membrane-less electrolyzer ( $\mu$ ME) improves because of increased mass transfer by short residence time and short radial diffusion.<sup>13</sup> The kinetics of water electrolysis in the  $\mu$ ME increase due to the high surface-to-volume ratio at the microscale. In a previous work, it was shown that the flexibility in the choice of pH for the  $\mu$ ME improved the kinetics of water electrolysis by utilizing the electrochemical neutralization energy arising from the asymmetric electrolyte (acidic catholyte and alkaline anolyte) configuration.<sup>14</sup>

As microfluidic channels operate in the laminar regime, greater flow control can be achieved, rendering the  $\mu$ ME membraneless. The catholyte–anolyte interface behaves as a virtual membrane in the  $\mu$ ME facilitating ion transfer across the electrode.<sup>15</sup> However, one challenge in the  $\mu$ ME's membraneless operation is the gas product cross-over across the electrode. The intermixing of the gas products in the  $\mu$ ME can be averted by optimizing the flow rate of the electrolyte and the interelectrode distance to control the position, trajectory, and coalescence of the gas bubble in the microchannel.<sup>16,17</sup>

The catalyst accounts for a 25% cost of manufacturing the water electrolyzer.<sup>18</sup> The advancements in the catalyst activity and manufacturing process can address the issue of the high catalyst cost. The development of the  $\mu$ ME has lagged due to the poor performance of catalysts for water electrolysis.<sup>16,17,19</sup> The use of expensive catalysts (Pt, De Nora S.p.A. mixed oxide catalyst) considerably increases manufacturing costs, limiting the applicability of the  $\mu$ ME for scale-up.

The synthetic protocols of the catalysts with benchmarking efficiencies are incompatible with the microfabrication process of membraneless technology.<sup>5,20–22</sup> The catalysts for the  $\mu$ ME must fulfill the following criteria: inexpensive, bifunctional for overall water splitting, that is, capable of hydrogen and oxygen evolution reaction (HER and OER), customizable with added functionality, and amenable for manufacturing as microelectrodes. It is imperative to have a bifunctional catalyst for

the  $\mu$ ME because incorporating two different catalysts for HER and OER will require an additional step in the manufacturing, which further adds to the complexity of the microfabrication process.

Plasma-assisted functionalization/activation of the catalyst is a promising strategy compatible with microelectrode fabrication. A few works of the literature are available on the electrochemical performance of plasma-assisted activation of earth-abundant metals for water electrolysis.<sup>23–34</sup> Nevertheless, they fail to satisfy the criteria mentioned above, as they are not readily compatible with microelectrode fabrication.

Herein, we address challenges in both catalyst performance and manufacturability by demonstrating the fabrication and performance evaluation of a bifunctional nickel nitride/nickel ( $\text{Ni}_3\text{N}/\text{Ni}$ ) electrocatalyst in a microfluidic alkaline membrane-less electrolyzer ( $\mu$ AME) for overall water splitting. The bifunctional property is vital to reduce manufacturing costs by eliminating an additional microfabrication step to introduce two distinct catalysts for HER and OER. The catalyst is made bifunctional by chemical functionalization in which a sputtered thin film of Ni (400 nm) is activated under ammonia ( $\text{NH}_3$ ) plasma in a plasma-enhanced chemical vapor deposition (PECVD) reactor. The plasma exposure time and temperature are varied to produce a series of catalysts. The effect of nitridation in  $\text{Ni}_3\text{N}/\text{Ni}$  by  $\text{NH}_3$  plasma on the physical and electrochemical properties of water electrolysis is analyzed by comparison with a bare Ni electrocatalyst. The enhanced performance of the bifunctional  $\text{Ni}_3\text{N}/\text{Ni}$  catalyst for water electrolysis in alkaline pH is compared with that of Pt, as Pt is extensively used in microfabrication. The electrochemical activity for water electrolysis is evaluated by performing the half-cell study using linear sweep voltammetry (LSV), cyclic voltammetry (CV), potentiometric electrochemical impedance spectroscopy (PEIS), and chronoamperometry (CA).

The  $\text{Ni}_3\text{N}/\text{Ni}$  bifunctional catalyst is incorporated in the  $\mu$ AME, and the overall water splitting performance of the device in the two-electrode configuration is evaluated by LSV, PEIS, and CA. The flow rate in the membraneless device is optimized to achieve the desired gas product separation.  $\text{H}_2$  and  $\text{O}_2$  are collected from the bifurcation of the Y-shaped microchannel and analyzed by gas chromatography (GC) to estimate gas intermixing in the membraneless operation. To our knowledge, this is the first study illustrating the adoption of microfabrication techniques to develop the  $\text{Ni}_3\text{N}/\text{Ni}$  bifunctional catalyst and evaluating the overall water splitting performance of this catalyst in a  $\mu$ AME.

## 2. EXPERIMENTAL SECTION

**2.1. Catalyst Fabrication.** The catalyst thin films were deposited by DC sputtering on Borofloat glass substrates. Ni, Pt, and Ti sputtering targets (2" diameter  $\times$  0.125" thick) were procured from Kurt J. Lesker, Inc. All processes for catalyst synthesis were done in class 100 and class 10k cleanrooms. The Borofloat glass substrates were Piranha-cleaned (3:1 solution of concentrated  $\text{H}_2\text{SO}_4$  and 30%  $\text{H}_2\text{O}_2$ ), rinsed sequentially in deionized water (DI), acetone, and isopropyl alcohol (IPA), and then dried to remove moisture.

A uniform Pt thin film (50, 100, and 400 nm) on the Ti sacrificial layer was obtained by DC sputtering at a base pressure of  $1.4 \times 10^{-6}$  mTorr and argon pressure of 7 mTorr. The samples with Pt thicknesses 50, 100, and 400 nm were named Pt:50, Pt:100, and Pt:400, respectively. The DC sputtering power for Pt was 70 and 300 W for Ti. Sputtering durations for Pt:50, Pt:100, and Pt:400 were 2, 4, and 16 min, respectively. The argon was supplied at 20 sccm to create the plasma for sputtering. The substrate was rotated at 60 rpm during sputtering to achieve a uniform deposition.

$\text{Ni}_3\text{N}/\text{Ni}$  was synthesized by sputtering Ni (400 nm) on a Borofloat substrate, followed by nitridation in an  $\text{NH}_3$  plasma for 15 min to achieve the desired functionality. Ni was sputtered by DC sputtering at 300 W power and 35 min with a substrate rotation of 60 rpm to obtain a uniform thin film of 400 nm on the substrate. The base pressure was  $1.4 \times 10^{-6}$  mTorr, and argon pressure during deposition was maintained at 7 mTorr with a 20 sccm flow rate. The nitridation of the Ni sputtered substrate was done in a PECVD reactor (Trion Technology, Inc). Samples were exposed to a  $\text{NH}_3$  plasma for 15 min at 400 mTorr pressure, 220 W RF power, and 350  $^\circ\text{C}$ . The flow rate of  $\text{NH}_3$  to the reactor was 20 sccm. The obtained sample was referred to as NN15:350 for simplicity. To determine the effect of plasma exposure time and temperature on the properties of  $\text{Ni}_3\text{N}/\text{Ni}$ , a few other samples were also prepared, which was referred to as NN30:350 (30 min  $\text{NH}_3$  plasma, 350  $^\circ\text{C}$ ), NN45:350 (45 min  $\text{NH}_3$  plasma, 350  $^\circ\text{C}$ ), NN15:400 (15 min  $\text{NH}_3$  plasma, 400  $^\circ\text{C}$ ), NN15:450 (15 min  $\text{NH}_3$  plasma, 450  $^\circ\text{C}$ ), and NN15:350 $\text{N}_2$  (15 min  $\text{N}_2$  plasma:350  $^\circ\text{C}$ ).

**2.2. Physicochemical Characterization.** **2.2.1. X-ray Powder Diffraction.** The phase structure and crystalline feature of materials were determined using X-ray diffraction (XRD) spectra acquired on a Bruker D8 DISCOVER instrument using  $\text{Cu K}\alpha$  radiation (40 kV,  $\lambda = 0.15418$  nm) equipped with a LynxEYE 1-dimensional detector. The spectra were accumulated by maintaining a scan size of 0.02 $^\circ$ .

To validate increased crystallinity, the grain sizes of the samples were calculated from the (111) peak of Ni using the Scherrer equation

$$S = \frac{K\lambda}{\beta \cos \theta} \quad (1)$$

where  $S$  is the mean crystallite size,  $K$  is a dimensionless shape factor (assumed as 1),  $\lambda$  is the wavelength of X-ray (0.15418 nm for  $\text{Cu K}\alpha$  source),  $\beta$  is the full width at half of the maximum (fwhm) in radians, and  $\theta$  is the Bragg angle.  $\beta$  was calculated by Lorentzian fits of the (111) Ni peak.

**2.2.2. SEM and Energy-Dispersive X-ray Spectroscopy.** The rough surface morphological attributes and the cross-section of the samples were observed by field-emission scanning electron microscopy (FE-SEM), using a Zeiss Sigma FESEM equipped with a Gemini column and operating at an accelerating voltage of 5 kV. The energy-dispersive X-ray (EDX) spectrometry elemental mapping was performed on a Zeiss Sigma FESEM w/ EDX & EBSD integrated with the Oxford AZtecSynergy system at 15 kV and 300 s acquisition time.

**2.2.3. X-ray Photoelectron Spectroscopy.** The surface and subsurface ( $\sim 10$  nm) chemical nature and oxidation state of constituting elements of materials were determined with X-ray photoelectron spectroscopy (XPS) recorded on an Axis-Ultra, Kratos Analytical instrument equipped with a monochromatic  $\text{Al K}\alpha$  source (15 kV, 50 W, photon energy of 1486.7 eV) under ultrahigh vacuum (UHV  $\sim 10^{-8}$  Torr). The C1s binding energy of adventitious hydrocarbon at  $\approx 284.8$  eV was used for referencing the binding

energy (BE) of all other elements (carbon correction). The acquired XPS data in .vms format were deconvoluted in various peak components using CasaXPS, and exported files were later plotted in Origin 2018. XPS depth profiling of the sample was undertaken to investigate the composition of the samples as a function of penetration depth. Measurements were done on a PHI VersaProbe III Scanning XPS Microprobe equipped with a flexible monatomic Ar ion beam, Ar, and C60 GCIB cluster ion guns.

**2.2.4. Electrochemical Analysis.** The electrochemical test for HER and OER activity of  $\text{Ni}_3\text{N}/\text{Ni}$  (NN15:350), Ni, and Pt was performed in a typical three-electrode configuration using an electrochemical workstation (Gamry Instruments Reference 3000). NN15:350, Ni and Pt as a working electrode, saturated silver–silver chloride electrode ( $\text{Ag}/\text{AgCl}/\text{sat. KCl}$ ) as a reference electrode, and Pt as a counter electrode were used in 1.0 M KOH electrolyte. The obtained potentials at the  $\text{Ag}/\text{AgCl}$  scale were converted to a reversible hydrogen electrode (RHE) scale by following expression,  $V_{\text{RHE}} = V_{\text{Ag}/\text{AgCl}} + 0.059 \text{ pH} + V_{\text{Ag}/\text{AgCl}}^0$ , where  $V_{\text{RHE}}$  is the voltage versus RHE,  $V_{\text{Ag}/\text{AgCl}}$  is the voltage versus  $\text{Ag}/\text{AgCl}/\text{sat. KCl}$  reference electrode, and  $V_{\text{Ag}/\text{AgCl}}^0 = 0.197$  V is the standard electrode potential at 25  $^\circ\text{C}$ . The current–voltage response was recorded by LSV at a scan rate of 20  $\text{mV s}^{-1}$  in the potential range of  $-1$  to  $+2.5$  V versus RHE.

To study the kinetics of the catalyst for HER and OER, the Tafel slopes for the catalysts were estimated from LSV curves by a linear fit to the Tafel equation:  $\eta = b \log|j| + a$ , where  $\eta$  is the overpotential,  $j$  is the current density,  $b$  is the Tafel slope, and  $a$  is the constant. PEIS to obtain the Nyquist plot was recorded in the frequency range of 100 kHz to 0.1 mHz at a 10 mV alternating current (AC) amplitude. The double-layer capacitance ( $C_{\text{dl}}$ ) was estimated for NN15:350 and Ni catalysts using CV at various scan rates (10–100  $\text{mV s}^{-1}$ ) in the potential range of 0.8–1.2 V versus RHE. CA was performed on NN15:350 at a constant applied voltage of  $-0.3$  and 1.7 V versus RHE for HER and OER, respectively, for 16 h.

**2.3.  $\mu\text{AME}$  Fabrication and Performance Evaluation.** The steps for the fabrication of the  $\mu\text{AME}$  are depicted in Figure 2. Soft lithography was used to fabricate a polydimethylsiloxane (PDMS)

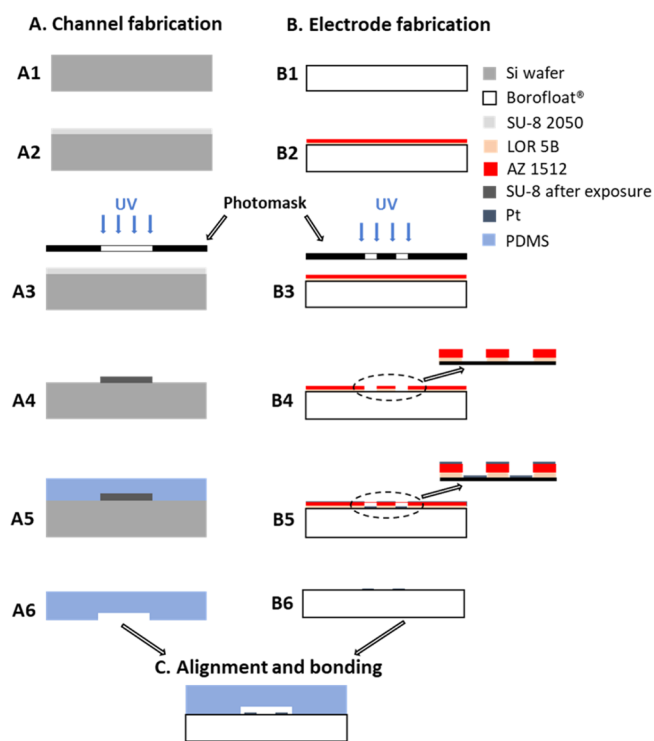


**Figure 2.** Steps for the fabrication of the  $\mu\text{AME}$ : (A) channel fabrication, (B) electrode fabrication, and (C) alignment and bonding.

microchannel of 100  $\mu\text{m}$  depth. The microchannel template was made on Si prime wafer. The Si wafers (UniversityWafer, Inc, USA) were cleaned with piranha solution (3:1 solution of  $\text{H}_2\text{SO}_4$  and 30%  $\text{H}_2\text{O}_2$ ), rinsed with acetone and IPA to remove any organic residue, and dried using  $\text{N}_2$  (Figure 2A1). A negative photoresist (PR) (SU8 2050, MicroChem) was spin-coated on the cleaned Si wafer to a thickness of  $\sim 100 \mu\text{m}$  and soft baked at 65  $^\circ\text{C}$  for 6 min and at 95  $^\circ\text{C}$  for 30 min (Figure 2A2).

The negative PR coated on the Si wafer was exposed to UV through a photomask by a mask aligner (SUSS MA6, MicroTec) to transfer the channel design (Figure 2A3). The UV exposure was followed by post-exposure baking at 65  $^\circ\text{C}$  for 6 min and 95  $^\circ\text{C}$  for 12 min. After baking, the PR was developed in the MicroChem SU8 developer for 20 min, removing the excess PR, followed by rinsing with IPA and DI water several times and dried using an  $\text{N}_2$  gun. The patterned Si wafer with the microchannel design served as a template for microchannel fabrication (Figure 2A4).

The PDMS prepolymer and curing agent (Sylgard 184, Dow Corning) were mixed in a 10:1 ratio and degassed in a vacuum oven. PDMS was then poured on the patterned Si wafer in a Petri dish and cured at 80  $^\circ\text{C}$  for 1 h (Figure 2A5). After curing, the PDMS was carefully peeled from the Si wafer. The double-Y microchannel design was engraved on the PDMS, having a length and width of 15 mm and 800  $\mu\text{m}$ , respectively. Provision for inlet and out of the fluid was made by cutting holes of 2 mm diameter (Figure 2A6).

A lift-off process was used to pattern the Pt and NN15:350 electrodes on Borofloat (Figure 2B). The Borofloat glass substrate was cleaned in Piranha solution, rinsed in DI water, acetone, and IPA, and dried at 100  $^\circ\text{C}$  to remove moisture (Figure 2B1). The pristine Borofloat glass was placed in the HMDS (hexamethyldisilazane) oven for 15 min at 150  $^\circ\text{C}$ . A monolayer of HMDS was formed on the Borofloat substrate, which makes the surface of the substrate hydrophobic and promotes PR adhesion. The substrate was then spin-coated with  $\sim 1.7 \mu\text{m}$  of LOR 5B resist (MicroChem) and baked at 115  $^\circ\text{C}$  for 90 s. The LOR 5B provides an undercut for successful lift-off patterning of metals. The substrate was cooled for 10 min and spin-coated with a positive PR AZ 1512 ( $\sim 1.1 \mu\text{m}$ , MicroChemicals GmbH) followed by soft baking at 100  $^\circ\text{C}$  for 60 s (Figure 2B2). The PR-coated substrate was selectively exposed to UV through the photomask by a mask aligner to pattern the electrode design (Figure 2B3). The UV-exposed substrate was immersed in the AZ Developer 1:1 (50 s) and MF 319 (5 s) (to develop AZ 1512 and LOR 5B, respectively) to get a design patterned for the deposition of microelectrodes (Figure 2B4).

The patterned glass substrate was metalized through the openings in the PR (Figure 2B5) by sputtering a uniform thin film of 10 nm Ti and 100 nm Pt by DC sputtering (Kurt J. Lesker) using the method described earlier. The metallization of the glass substrate for NN15:350 electrodes was done by depositing a thin film of Ni (400 nm) followed by nitridation in  $\text{NH}_3$  plasma, as described earlier. The excess PR on the metalized glass substrate was removed by lift-off using acetone to obtain the anode and cathode for the  $\mu\text{AME}$  application (Figure 2B6). The electrode has a length of 15 mm, width of 300  $\mu\text{m}$ , and interelectrode distance of 150  $\mu\text{m}$ .

The glass substrate patterned with Ni electrodes was subjected to  $\text{NH}_3$  plasma to achieve nitridation, as discussed in the experimental and synthesis section. To form devices, the PDMS with microchannel design and the electrode-patterned substrates (Pt, and NN15:350) were exposed to  $\text{O}_2$  plasma, aligned under the microscope to make certain that the electrodes lie inside the microchannel, and irreversibly bonded by sticking them together to form the Si–O–Si bond between PDMS and the glass slide (Figure 2C). Approximately, a 13% reduction in the fabrication cost of the  $\mu\text{AME}$  was achieved by employing the Ni-based bifunctional catalyst compared to Pt.

The experimental setup used to measure the characteristics of the  $\mu\text{AME}$  is shown in Figure S1. The  $\mu\text{AME}$  was placed under a microscope (VHX-700F, Keyence Canada Inc.) equipped with a camera that provides a qualitative visual tool for analyzing the two-phase flow of gas and the electrolyte. The transparent PDMS top cover allows for the observation of the flow in the microchannel. The

videos were recorded at 16 fps with 300 $\times$  magnification. The  $\mu\text{AME}$  was operated in an orientation perpendicular to the gravity. The effect of gravity in this position was safely ignored, as Froude's number was estimated to be higher than 1 (ratio of inertia force to gravity force, Table S1). The electrolyte (1.0 M KOH, AR grade, Thermo Fisher Scientific, USA) was made in DI water. A pulsation-free syringe pump (KD Scientific) was employed to supply the electrolyte to the  $\mu\text{AME}$  at the desired flow rate.

The electrolyte flow rate (0.8–1.2  $\text{mL min}^{-1}$ ) in the microchannel was optimized to achieve gas separation under an applied voltage of up to 2.5 V. The typical characteristics of fluid flow in a microchannel, such as viscous flow and convective diffusion, were characterized by the estimation of the electrolyte flow rate and geometry-dependent dimensionless numbers, the Reynolds number ( $Re$ ), and Peclet number ( $Pe$ ).

The  $\mu\text{AME}$  performance with either Pt or NN15:350 electrodes was examined by electrochemical characterization (LSV, PEIS, and CA) using a potentiostat (Gamry Instrument Reference 3000). Tungsten microelectrode probes were employed to connect the potentiostat to the microfluidic electrolyzer. An inverted pair of calibrated glass burettes with septum caps assisted in gas product collection from the outlet of the Y-shaped bifurcation of the  $\mu\text{AME}$ . The tube fittings used were ensured to be gas-tight to prevent product loss by leakage. A gas chromatograph (Agilent Technologies, 6890N Network GC System) with a thermal conductivity detector was employed to analyze the product purity and qualitatively estimate product cross-over to establish the efficient operation of the  $\mu\text{AME}$ .

### 3. RESULTS AND DISCUSSION

**3.1. Physical Analysis.** The XRD spectra of the Pt thin film (denoted as Pt:100, Figure S2) show intense signature peaks at 39.28 $^\circ$  (111) along with a weak peak at 45.86 $^\circ$  (200) and 67.14 $^\circ$  (220) for the face-centered cubic structure of metallic Pt (ICDD # 00-004-082).<sup>35</sup> The presence of a strong (111) peak suggests preferred (111) crystal orientation with the lowest surface energy on the sputtered Pt thin film.

Ni thin films were exposed to ammonia plasma for 15, 30, and 45 min in a temperature range of 350–450  $^\circ\text{C}$ . The samples are referred to as NN15:350 (15 min  $\text{NH}_3$  plasma, 350  $^\circ\text{C}$ ), NN30:350 (30 min  $\text{NH}_3$  plasma, 350  $^\circ\text{C}$ ), NN45:350 (45 min  $\text{NH}_3$  plasma, 350  $^\circ\text{C}$ ), NN15:400 (15 min  $\text{NH}_3$  plasma, 400  $^\circ\text{C}$ ), NN15:450 (15 min  $\text{NH}_3$  plasma, 450  $^\circ\text{C}$ ), and NN15:350N<sub>2</sub> (15 min  $\text{N}_2$  plasma:350  $^\circ\text{C}$ ).

The crystallinity and phase structure of untreated Ni and the nitrided films were determined using an XRD pattern (Figure 2a). The XRD spectra of the Ni film displayed three characteristic peaks of the face-centered cubic nickel metal at 44.45 $^\circ$ , 51.95 $^\circ$ , and 76.35 $^\circ$ , which are assigned to (111), (200), and (202) planes, respectively (ICDD # 00-004-0805).<sup>36</sup> After nitridation of the Ni film in the  $\text{NH}_3$  plasma, a few new XRD peaks emerged at 38.9 $^\circ$ , 58.7 $^\circ$ , and 70.5 $^\circ$ , which can be ascribed to (110), (112), and (300) planes of hexagonal nickel nitride ( $\text{Ni}_3\text{N}$ ), respectively, as reported in the literature (ICDD # 00-010-0280).<sup>24,37</sup> As the penetration depth of X-rays is high, XRD signals are mainly populated from the bulk of the material. The low peak intensity of  $\text{Ni}_3\text{N}$  suggests that only a tiny fraction of Ni (likely at the surface of the sample) was functionalized with nitride groups. Interestingly, for the samples prepared via nitridation in  $\text{NH}_3$  plasma at 350  $^\circ\text{C}$  treated from 15 to 45 min, the nitride peak was visible, verifying the nitridation of samples, while for samples prepared at 400 and 450  $^\circ\text{C}$ , no trace of nitride peaks was seen, suggesting that high-temperature plasma treatment prevents nitridation. It has been shown in the literature that, at high temperatures,  $\text{NH}_3$  is degraded into nitrogen and hydrogen on

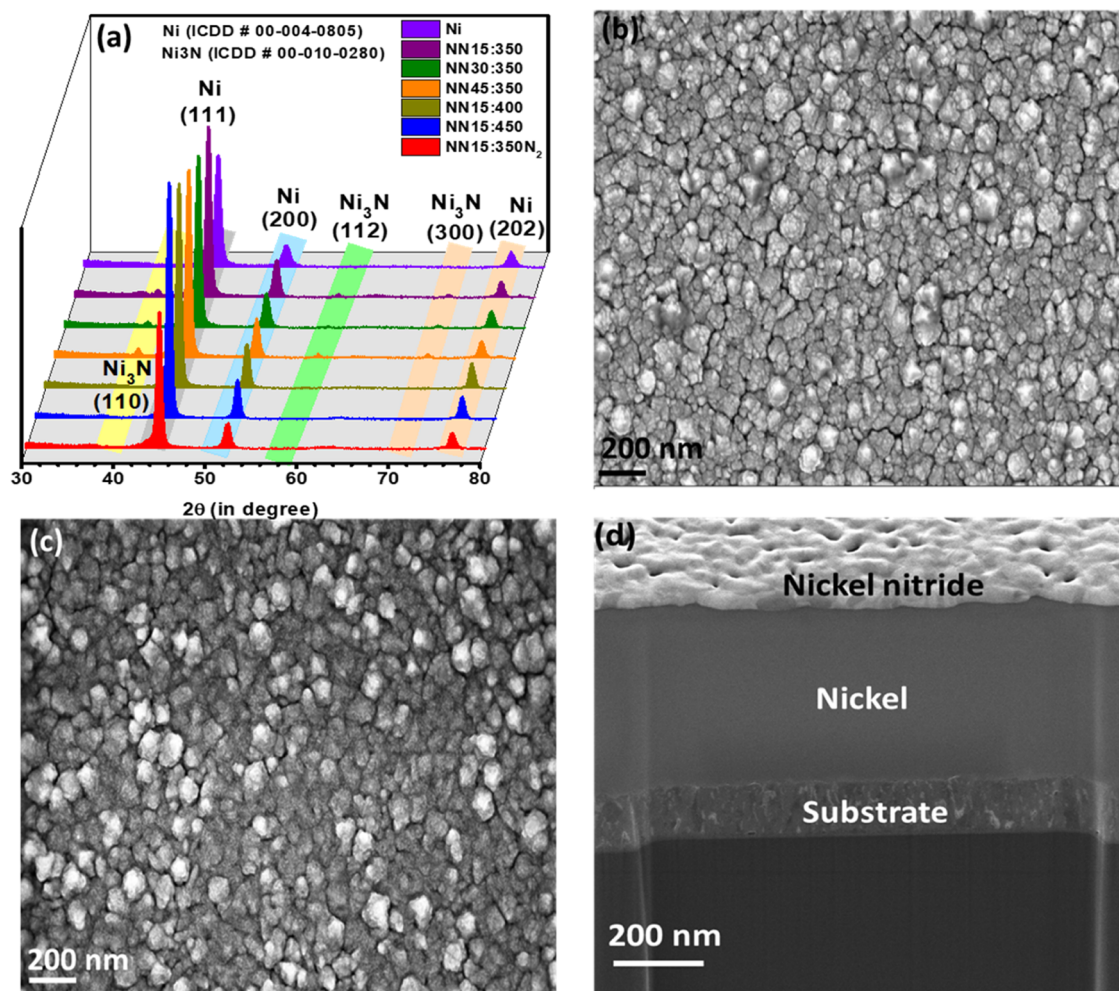


**Figure 3.** (a) XRD spectra of Ni, NN15:350, NN30:350, NN45:350, NN15:400, NN15:450, and NN15:350N<sub>2</sub> and FE-SEM images of (b) bare Ni, (c) NN15:350, and (d) NN15:350 cross-sectional view.

metallic surfaces, which results in the absence of any adsorbed NH<sub>3</sub> on the sample's surface to participate in nitridation reaction.<sup>38,39</sup> In addition, the sample prepared under nitrogen plasma (rather than ammonia plasma) at 350 °C exhibited no Ni<sub>3</sub>N peak, suggesting that the presence of NH<sub>3</sub> rather than N<sub>2</sub> was critical to the plasma-assisted nitridation process.

The intensity of the Ni peaks increased with the nitridation temperature, which may result from enhanced crystallization (Figure S2a). The obtained crystallite grain sizes for Ni, NN15:350, NN30:350, NN45:350, NN15:400, NN15:450, and NN15:350N<sub>2</sub> were found to be 16.99, 19.72, 19.18, 20.01, 20.48, 20.50, and 19.03 nm, respectively (Figure S2b). The crystallite size of samples prepared by nitridation under N<sub>2</sub> plasma at 350 °C was relatively small, attributed to the absence of any nitridation. The peak intensity for NN15:350 (red line) and 3-NN30:350 (blue line) is almost identical, as shown in Figure S3. However, the peak width in both cases is different (Figure S4a). The crystallite size determination using the Scherrer equation (eq 1) includes full width half maximum, fwhm, of the peak of interest. Therefore, the crystallite size is inversely proportional to the fwhm. After the Lorentzian fit, the fwhm for NN15:350 and NN30:350 was calculated to be 0.4544 and 0.4692, respectively, translated to 19.72 and 19.18 nm crystallite sizes (Figure S4b). The higher value of fwhm for NN30:350 suggests a smaller crystallite size.

The surface morphological features of the materials were observed with FE-SEM (Figure 3b–d). The FE-SEM image of the Pt:100 thin film exhibits uniform distribution and a compact layer on the surface (Figure S5a). The FE-SEM image of NN15:350 (Figure 3c) shows a less rough surface than the bare Ni sample (Figure 3b), with cracked and erupted features. The cross-sectional FE-SEM of the NN15:350 sample shows a distinct interface of Ni and Ni<sub>3</sub>N and suggests that nitridation occurs on the surface of Ni.

EDX elemental mapping revealed uniform Pt distribution on the surface with no trace of the Ti sacrificial layer (Figure S5b). EDX elemental mapping of NN15:350 for Ni and N elements shows an even distribution element throughout the samples, reflecting the presence of Ni<sub>3</sub>N (Figure S3a–c). However, the density of mapping dots for N was much smaller than for Ni, showing that Ni<sub>3</sub>N was a relatively minor constituent of the samples and metallic Ni still dominates. A composite of the mapped image shows overlapped points due to a well-constructed Ni<sub>3</sub>N surface (Figure S3c). EDX spectra were used to calculate the atomic percentage of Ni and N to be 94.4 and 5.6%, respectively (Figure S3d). The obtained N at % value was in close agreement with the value obtained from the XPS spectra (Figure 3).

The chemical composition and nature of binding from the oxidation state of constituting elements were determined using

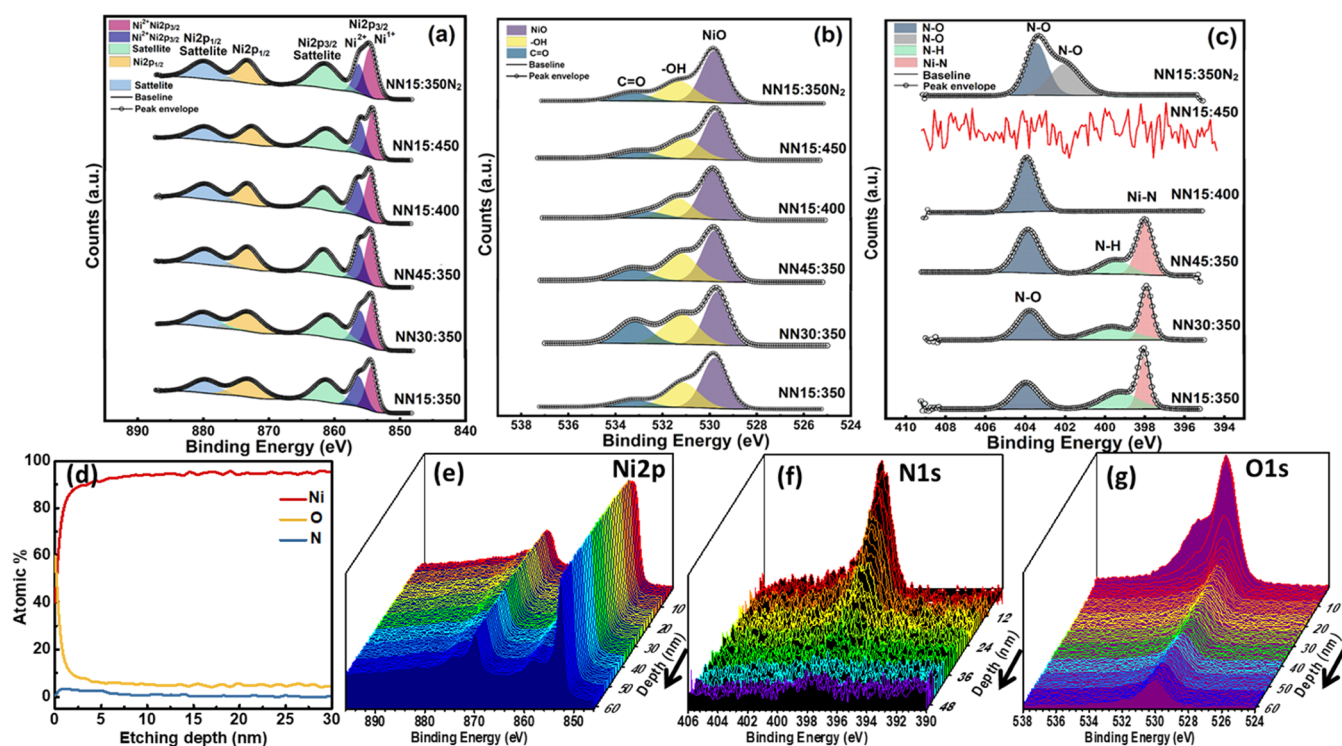


**Figure 4.** Core-level high-resolution XPS spectra of NN15:350, NN30:350, NN45:350, NN15:400, NN15:450, and NN15:350N<sub>2</sub> in the (a) Ni 2p (b) O 1s, and (c) N 1s region. (d) XPS depth profile for NN15:350 showing the change in Ni, O, and N elemental composition as a function of depth up to 30 nm and relative XPS spectra in the (e) Ni 2p, (f) N 1s, and (g) O 1s region.

XPS (Figure 4). The XPS survey scan of the Ni samples after nitridation under various conditions displayed all the core-level (Ni: Ni 2p, O 1s, and N 1s) and inner- and outer-core-level (NiLLM, OKLL, Ni 3s, and Ni 3p) peaks of constituting elements (Figure S4).

The high-resolution XPS multiplex spectra of NN15:350 samples in the Ni 2p region displayed two significant peaks, Ni 2p<sub>3/2</sub> and Ni 2p<sub>1/2</sub> peaks, and their shake-up satellite peaks (arising from the spin-orbit splitting of the 2p orbital) (Figure 4a). The Ni 2p peak could be deconvoluted into five components centered at BE values of 854.08, 856.03, 861.31, 872.59, and 879.93 eV. The XPS peak at BE  $\approx$  854.08 eV was assigned to Ni<sup>+</sup> present in Ni<sub>3</sub>N, while another peak centered at 856.03 eV was assigned to Ni<sup>2+</sup> present as either oxide or hydroxide (NiO or Ni(OH)<sub>2</sub>).<sup>40,41</sup> The broad peak component located at 861.31 eV was assigned to the Ni2p<sub>3/2</sub> shake-up satellite peak, originating from the excitation of the high-spin nickel ions.<sup>42</sup>

The peaks observed at 872.59 and 879.93 eV correspond to Ni 2p<sub>1/2</sub> and Ni 2p<sub>1/2</sub> satellite peaks, respectively. For all samples (NN30:350, NN45:350, NN15:400, NN15:450, and NN15:350N<sub>2</sub>), the BE values corresponding to Ni<sup>1+</sup> (due to NiO) and Ni<sup>2+</sup> (due to Ni(OH)<sub>2</sub>) remain the same. The O 1s XPS spectra of each of the samples showed three peak components located at 529.84, 531.24, and 533.14 eV (Figure 4b). The major peak at 529.84 eV originated from oxidized nickel present as oxide and hydroxide (NiO and Ni(OH)<sub>2</sub>).<sup>24</sup> Two shoulder peaks centered at 531.24 and 533.14 eV were corroborated to surface-adsorbed -OH and adventitious carbonyls (C=O) of surface adsorbed organics, respectively.

Deconvoluted HR-XPS of NN15:350 samples in the N1s region displayed three peak components centered at 398.04, 399.50, and 403.94 eV (Figure 4c). The peak component at BE

$\approx$  398.04 eV was assigned to Ni metal-bonded Ni-N nitrogen in Ni<sub>3</sub>N. In contrast, another shoulder peak at 399.50 eV was observed due to residual N-H nitrogen added on the sample surface during the NH<sub>3</sub> plasma treatment.<sup>23</sup> A well-separated peak at 403.94 eV originated from the oxidized N-O oxygens.<sup>43</sup> It can be seen from Figure 4c that samples prepared using a NH<sub>3</sub> plasma treatment at 350 °C (NN15:350, NN30:350, and NN45:350) demonstrated the Ni-N peak to Ni<sub>3</sub>N.<sup>44,45</sup> As the temperature was increased to 400 °C (NN15:400), the Ni-N and NH peak disappeared, which may be due to the fast desorption of nitrogen moieties from the surface of the sample at high temperature. However, some chemisorbed nitrogen was present on the sample in the N-O state. A further rise in temperature to 450 °C (NN15:450) restricted adsorption of NH<sub>3</sub> on the sample surface, resulting in the absence of any nitrogenous functionalities in the N 1s spectra of the sample. The Ni-N peak was absent in the N<sub>2</sub> plasma-treated sample (NN15:350N<sub>2</sub>), suggesting that N<sub>2</sub> plasma treatment does not result in nitridation of the samples. However, N-O peaks were present in the NN15:350N<sub>2</sub> samples, which might arise due to the reaction of N<sub>2</sub> with surface oxygen groups at a higher temperature to produce oxidized N-O species. For the NN15:350N<sub>2</sub> sample, no peak for any nitrogenous species was present, implying that elevated temperature is crucial to promote the reaction of N<sub>2</sub> with surface oxygen functionalities. The NN15:450 sample prepared under NH<sub>3</sub> plasma at 450 °C also does not show any trace of nitride. Nevertheless, a peak due to N-H was observed, revealing that at this temperature, NH<sub>3</sub> chemisorbed on the Ni surface, but dehydrogenation did proceed.<sup>46</sup>

The XPS depth profile of the NN15:350 sample was measured to further characterize the surface nitridation and investigate the compositional change at various penetration

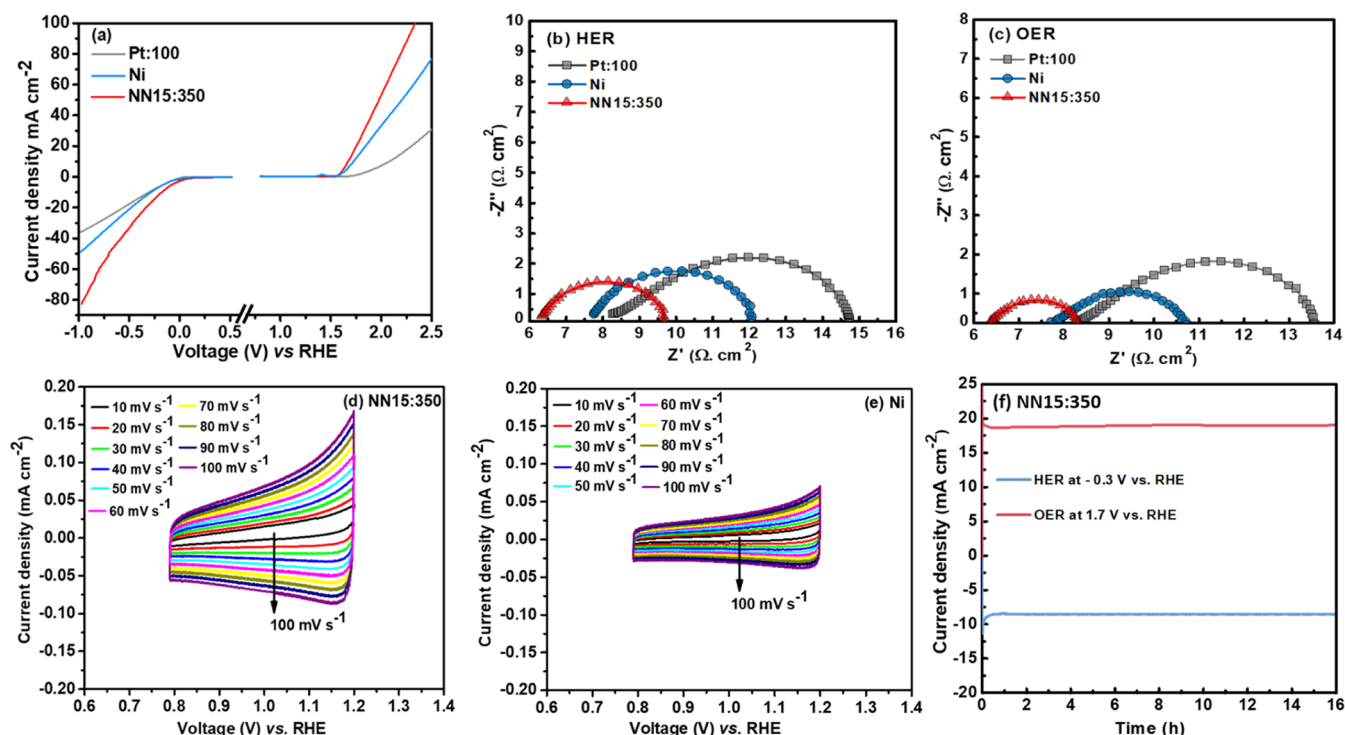


**Figure 5.** (a) LSV curves for HER and OER, PEIS for (b) HER and (c) OER activity of Pt, Ni, and NN15:350, and CV at different scan rates in the non-faradaic region for (d) NN15:350, (e) Ni, and (f) CA for NN15:350 at voltages corresponding to 10 mA cm<sup>-2</sup>.

depths. It can be seen from Figure 4d that the nitrogen content of the sample was 3.25% at the surface; this content gradually decreased, as the penetration depth increased and then completely disappeared at 15 nm (Figure 4d). Furthermore, the XPS spectra collected at various penetration depths demonstrate that nitrogen signals were dominated with Ni–N nitrogens, suggesting that only a tiny fraction of surface nitrogens was oxidized to N–O as evidenced from regular XPS (Figure 4f). Additionally, the Ni 2p depth profile shows the content of Ni increased from 40 to 91 at. % up to a depth of 5 nm and then reached a constant value. This confirms that surface Ni was mainly present as nitride and oxide (Figure 4d,e). The O 1s depth profile demonstrates a steep decrease in oxygen percentage (59–6 at. % at 5 nm), where the decline in the oxygen content coincides with the increasing Ni content (Figure 4d). As expected, the –OH and C=O peaks were limited to few nanometers, validating the presence of adventitious oxygens on the surface (Figure 4g). Over the first 1 nm, the atomic percentage of Ni increased from 40 to 81, while O decreased from 59 to 14 and N increased from 0.48 to 3.25, indicating that oxygen was confined to the top 1–2 nm of the sample surface, while nitridation reached a depth of up to 15 nm. All of these results validate the presence of a well-constituted Ni<sub>3</sub>N surface.

To probe the existence of surface Ni in oxide and nitride states, the XPS depth profile spectra of NN15:350 in the etching time range of 0–120 s with a time delay of 30 s were plotted (Figure S8). The O 1s spectra of the sample before etching (0 s) show the presence of adventitious –OH and C=O oxygens, which gradually decrease during etching and completely disappeared after 120 s. However, the XPS peak component associated with Ni–O lattice oxygens remains almost identical, suggesting that surface Ni was present in the oxide state (Figure S8a). Similarly, the N 1s spectra of

NN15:350 show complete diminution of N–O and N–H peaks, verifying that N signals were dominated by Ni–N nitrogens of Ni<sub>3</sub>N (Figure S8b). It can be seen that Ni–O signals were confined to the topmost layer of the sample, signifying coverage of the sample surface with adventitious oxygens.

**3.2. Electrochemical Analysis.** The electrocatalytic activity of the bifunctional NN15:350 catalyst was evaluated by using the material as a working electrode in a typical three-electrode configuration. For comparison, Ni, NN15:350, and Pt catalysts were tested under identical conditions. The HER and OER performances of the catalysts were investigated by performing LSV at a scan rate of 20 mV s<sup>-1</sup>, and the obtained results are shown in Figure 5a.

For HER, a current density of 10 mA cm<sup>-2</sup> was achieved at overpotentials ( $\eta_{10,HER}$ ) of 178, 283, and 306 mV for NN15:350, Ni, and Pt:100 (Pt thickness 100 nm), respectively. To achieve a current density of 50 mA cm<sup>-2</sup>, NN15:350 exhibited a smaller overpotential ( $\eta_{50,HER}$ ) of 699 mV as compared to Ni (993 mV). At the same time, Pt:100 displayed a reduced catalytic activity with a high overpotential of 980 mV required to attain a current density of only 35.86 mA cm<sup>-2</sup>. The depreciated value of Pt for HER can be related to the thickness used in the present study.

$\eta_{10,HER}$  for Pt varies as a function of the thickness (refer to Figure S5). The  $\eta_{10,HER}$  values for Pt:50 (Pt thickness 50 nm) and Pt:400 (Pt thickness 400 nm) were 480 and 194 mV, respectively. The overpotential of NN15:350 for HER was less than Pt with a thickness in the range of 50–400 nm. Pt:100 was used throughout the study for comparison, as 100 nm Pt thickness is typical in the microfabrication processes. The  $\eta_{10,HER}$  value of the Pt plate is 66 mV, which is the lowest value observed among all samples and thicknesses. However, the higher current density attained for HER using the Pt plate is

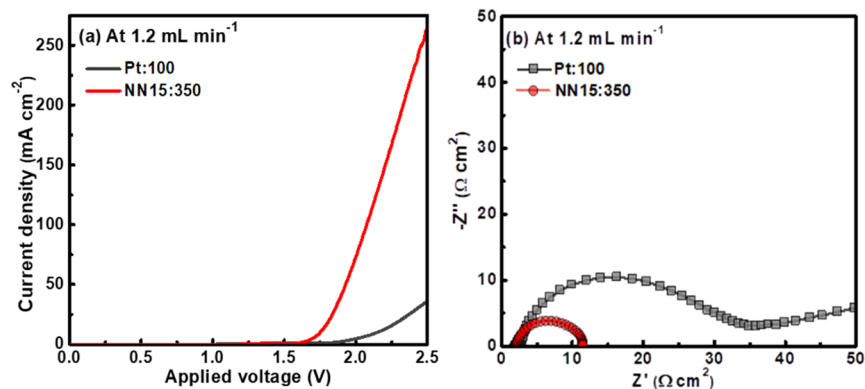


**Figure 6.** (a) Current–voltage response and (b) PEIS at  $1.2 \text{ mL min}^{-1}$  for Pt and NN15:350 for the  $\mu\text{AME}$ .

irrelevant, as it cannot be adopted for microfabrication. The HER activity of NN15:350 was compared with a few reported non-noble catalysts (Table S2) and showed enhanced performance compared to most catalysts.

NN15:350 demonstrated a higher current density than Ni and Pt:100 for OER in the entire potential range. The OER overpotential at a current density of  $10 \text{ mA cm}^{-2}$  ( $\eta_{10,\text{OER}}$ ) for NN15:350 (440 mV) was promising in comparison to Ni (498 mV) and Pt:100 (833 mV). The overpotential corresponding to  $50 \text{ mA cm}^{-2}$  current density ( $\eta_{50,\text{OER}}$ ) was 740 and 972 mV for NN15:350 and Ni, respectively, which is noticeably better than the OER catalytic performance of Pt:100 ( $30.86 \text{ mA cm}^{-2}$  at an overpotential of 1.27 V). The OER performance of NN15:350 was comparable to most of the other OER non-noble catalysts reported in the literature (Table S3). The substantial reduction in the overpotential for HER and OER in NN15:350 reflects the decisive role of nitrides and surface-grafted N–H induced by  $\text{NH}_3$  plasma.

The Tafel slopes for HER and OER derived from the polarization curves of NN15:350, Ni, and Pt:100 are present in Figure S6. The Tafel slope of  $46 \text{ mV dec}^{-1}$  for NN15:350 was lower than that of Ni ( $125 \text{ mV dec}^{-1}$ ) and Pt:100 ( $179 \text{ mV dec}^{-1}$ ), indicating the favorable HER catalytic property of NN15:350 in alkaline media. The alkaline HER on the transition metal (M) consists of two primary steps, the Volmer reaction ( $\text{M} + \text{H}_2\text{O} + \text{e}^- \leftrightarrow \text{M}-\text{H}_{\text{ads}} + \text{OH}^-$ ) in which an electron transfer process produces the adsorbed hydrogen, followed by an electrochemical desorption Heyrovsky reaction ( $\text{M}-\text{H}_{\text{ads}} + \text{H}_2\text{O} + \text{e}^- \leftrightarrow \text{H}_2 + \text{M} + \text{OH}^-$ ) or chemical desorption Tafel reaction ( $2\text{M}-\text{H}_{\text{ads}} + \text{H}_2\text{O} + \text{e}^- \leftrightarrow \text{H}_2 + 2\text{M}$ ). The Tafel slope of NN15:350 ( $46 \text{ mV dec}^{-1}$ ) was within the range of the theoretical values for the rate-determining Heyrovsky ( $40 \text{ mV dec}^{-1}$ ) and Volmer ( $120 \text{ mV dec}^{-1}$ ) step obtained from a HER kinetic model,<sup>47</sup> indicating that HER proceeds via the Volmer–Heyrovsky mechanism.

The OER following the electrochemical oxide path<sup>48</sup> involves the  $\text{OH}^-$  ion discharge ( $\text{M} + \text{OH}^- \leftrightarrow \text{MOH} + \text{e}^-$ ), the combination of  $\text{OH}^-$  with MOH ( $\text{MOH} + \text{OH}^- \leftrightarrow \text{MO} + \text{H}_2\text{O} + \text{e}^-$ ), and oxygen atom combination ( $2\text{MO} \leftrightarrow \text{O}_2 + 2\text{M}$ ) with the corresponding Tafel slopes of 118, 39, and  $14 \text{ mV dec}^{-1}$ , respectively. The OER Tafel slope of NN15:350 ( $63 \text{ mV dec}^{-1}$ ) was lower than that of Ni ( $130 \text{ mV dec}^{-1}$ ) and Pt:100 ( $202 \text{ mV dec}^{-1}$ ), signifying desirable NN15:350 OER activity and the combination of MOH as the rate-limiting step. The presence of nitrides, nitrogen-bonded hydrogen, and the intimate contact between  $\text{Ni}_3\text{N}$  and metallic Ni in NN15:350 allowed for faster charge transport and superior catalytic

activity as compared to Ni and Pt:100.<sup>24</sup> To investigate the structural changes after the OER reaction, XRD spectra on the optimum performing NN15:350 sample were obtained. It can be seen from Figure S12 that after the reaction, no change in the peak position was observed, suggesting that the sturdy crystalline structure was retained after the OER. However, the peak intensities were slightly decreased along with slight peak broadening, suggesting the reduction of crystallite size.

Further insights into the catalyst kinetics were obtained by electrochemical impedance spectroscopy (PEIS) (Figure 5b,c). The high-frequency intersections of the Nyquist plot on the real axis at the start of the semicircle curve represent the ohmic/solution resistance ( $R_\Omega$ ), which was 6.3, 7.7, and  $8.24 \text{ } \Omega \text{ cm}^2$  for NN15:350, Ni, and Pt:100 catalysts. The  $R_\Omega$  value for NN15:350 was lower as compared to Ni and Pt:100. The higher  $R_\Omega$  of Pt:100 compared to that of Ni can be attributed to the intrinsic bulk resistivity. The resistivity is  $10.5$  and  $6.93 \text{ } \Omega \text{ m} \times 10^{-8}$  for Pt and Ni, respectively.<sup>49</sup> Moreover, NN15:350 was annealed at  $350 \text{ }^\circ\text{C}$  in the PECVD reactor during synthesis, resulting in an increase in the crystallite grain size, thereby lowering the resistivity.<sup>50–52</sup> The low resistivity of NN15:350 allows for faster electron transport through the film leading to a lower  $R_\Omega$  compared to that of Ni and Pt, as reflected in Figure 5b,c.  $R_\Omega$  remains the same with the reaction kinetics of HER and OER. The semicircular arc of the Nyquist plot for both HER and OER was much smaller for NN15:350 than for Ni and Pt:100. The intersection of the semicircle on the real impedance axis at low frequency signifies charge transfer resistance ( $R_{\text{ct}}$ ) at the electrode–electrolyte interface. The HER  $R_{\text{ct}}$  was smaller for NN15:350 ( $9.6 \text{ } \Omega \text{ cm}^2$ ) than for either Ni ( $12 \text{ } \Omega \text{ cm}^2$ ) or Pt:100 ( $14.7 \text{ } \Omega \text{ cm}^2$ ), which implies faster electron transport for HER in NN15:350. The low-frequency inductance signifies the prevalence of the Volmer–Heyrovsky reaction, as the Volmer–Tafel reaction does not contribute to inductive behavior.<sup>53</sup>

$R_{\text{ct}}$  in OER demonstrated similar trends as for the HER, where a lower reaction barrier for oxygen generation was offered by NN15:350 ( $8.3 \text{ } \Omega \text{ cm}^2$ ) in contrast to Ni ( $10.7 \text{ } \Omega \text{ cm}^2$ ) and Pt:100 ( $13.5 \text{ } \Omega \text{ cm}^2$ ). The PEIS results align well with the observation of the smaller Tafel slope and superior HER/OER kinetics of the NN15:350 bifunctional electrocatalyst.

The effect of  $\text{NH}_3$  plasma nitridation on Ni to generate N–H moieties and the  $\text{Ni}_3\text{N}$ –Ni interface to exhibit a superior HER/OER activity of NN15:350 was evaluated by measuring the electrochemical double-layer capacitance ( $C_{\text{dl}}$ ). CV was performed at different scan rates ( $10$ – $100 \text{ mV s}^{-1}$ ) under a

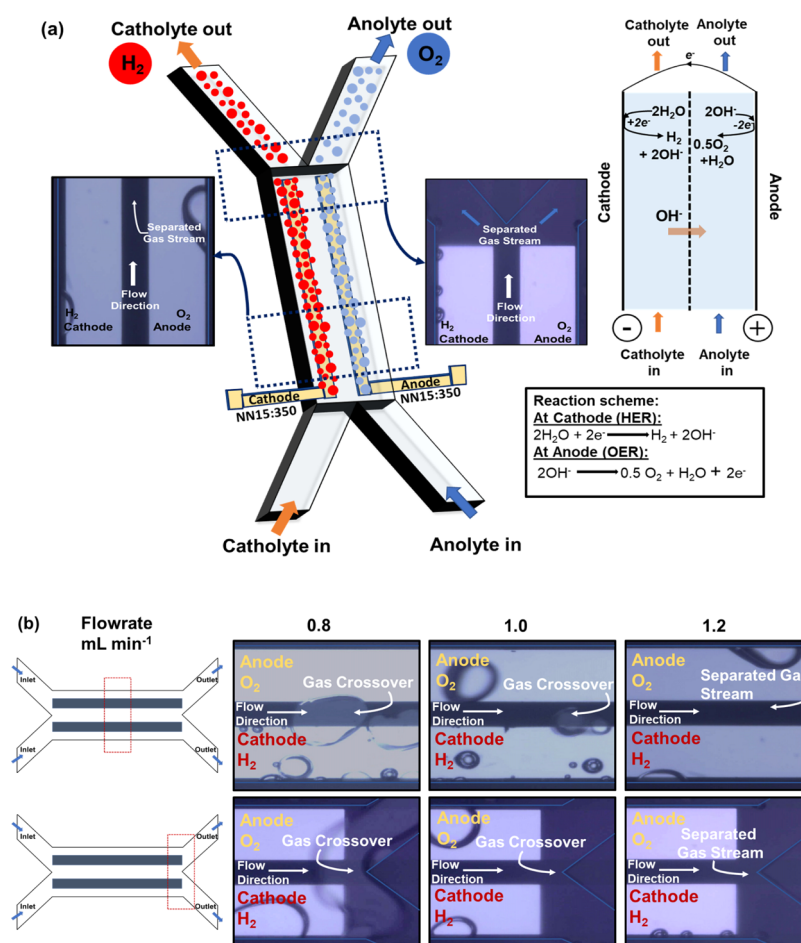


**Figure 7.** (a) Schematic representation of the  $\mu$ AME and (b) qualitative visual inspection of gas product separation with a varying flow rate in the  $\mu$ AME at an intermediate position and at the exit.

narrow voltage window in the non-faradaic reaction range for NN15:350 and Ni, as depicted in Figure 5d,e. A linear plot of the differential current ( $\Delta j$ ) between the anode and cathode (at 1 V vs RHE) at multiple scan rates (Figure S11) was used to estimate the slope, which was two times  $C_{dl}$ .  $C_{dl}$  of NN15:350 was  $0.7 \text{ mF cm}^{-2}$ , which was 2.33 times larger than Ni ( $0.3 \text{ mF cm}^{-2}$ ), indicating that NN15:350 has an increased number of electrochemical sites to perform HER/OER, owing to Ni–Ni<sub>3</sub>N at the interface and the functionality induced by NH<sub>3</sub> plasma.

Chronoamperometric (CA) measurements were used to assess the durability of NN15:350 toward HER and OER at a voltage corresponding to the cathodic and anodic current density of  $10 \text{ mA cm}^{-2}$  for 16 h (Figure 5f). A negligible drop in current density was observed for both HER and OER, revealing the excellent stability of the NN15:350 bifunctional electrocatalyst in alkaline media.

**3.3.  $\mu$ AME Performance Evaluation.** The current–voltage response (Figure 6a) was recorded to compare the electrochemical performance of the  $\mu$ AME with a Pt:100 electrocatalyst with that of the bifunctional NN15:350 electrocatalyst in an alkaline electrolyte at a flow rate of  $1.2 \text{ mL min}^{-1}$ . The onset potential of water electrolysis was estimated from the intersection of the two tangents on the curve where the current starts to increase. The onset potential for the  $\mu$ AME with Pt:100 electrodes was 1.98 V and that with NN15:350 electrodes was 1.7 V. The onset potential deviated

from the theoretical value (1.23 V) primarily due to the large overpotential associated with OER, ohmic and charge transfer resistances, and co-ions ( $K^+$ ) migration at the interface.<sup>54,55</sup>

The  $\mu$ AME with Pt:100 and NN15:350 electrodes required voltages of 2.14 V and 1.74 V, respectively, to split water at a  $10 \text{ mA cm}^{-2}$  current density. The current density of the  $\mu$ AME with NN15:350 electrodes was approximately 7.5 times more than that with Pt:100 electrodes at 2.5 V. The bifunctional NN15:350 electrocatalyst exhibited better performance than Pt:100 due to enhanced OER and HER activity in the alkaline electrolyte. A current density of  $200 \text{ mA cm}^{-2}$  was realized at 2.32 V for the  $\mu$ AME at room temperature with a less conductive electrolyte. This performance was comparable to that of a current state-of-art alkaline electrolyzer (30–40 wt % KOH electrolyte) with the anion exchange membrane, which typically operates at a temperature range of 60–80 °C at 1.8–2.4 V to achieve a current density of 200–400  $\text{mA cm}^{-2}$ .<sup>56</sup>

The ohmic resistance ( $R_{\Omega}$ ) and charge transfer resistance ( $R_{ct}$ ) of the  $\mu$ AME with Pt:100 and the bifunctional NN15:350 electrocatalyst at the  $1.2 \text{ mL min}^{-1}$  electrolyte flow rate were characterized by PEIS and are depicted in Figure 6b. PEIS was measured over a frequency range of 100 kHz–0.1 Hz, AC amplitude 10 mV, and DC voltage corresponding to  $10 \text{ mA cm}^{-2}$  current density. The contact resistance for making connections and the solution resistance contribute to  $R_{\Omega}$  in the  $\mu$ AME.  $R_{\Omega}$  of the  $\mu$ AME with the NN15:350 electrode was lower ( $1.88 \text{ } \Omega \text{ cm}^2$ ) than that with Pt:100 electrodes ( $2.60 \text{ } \Omega$

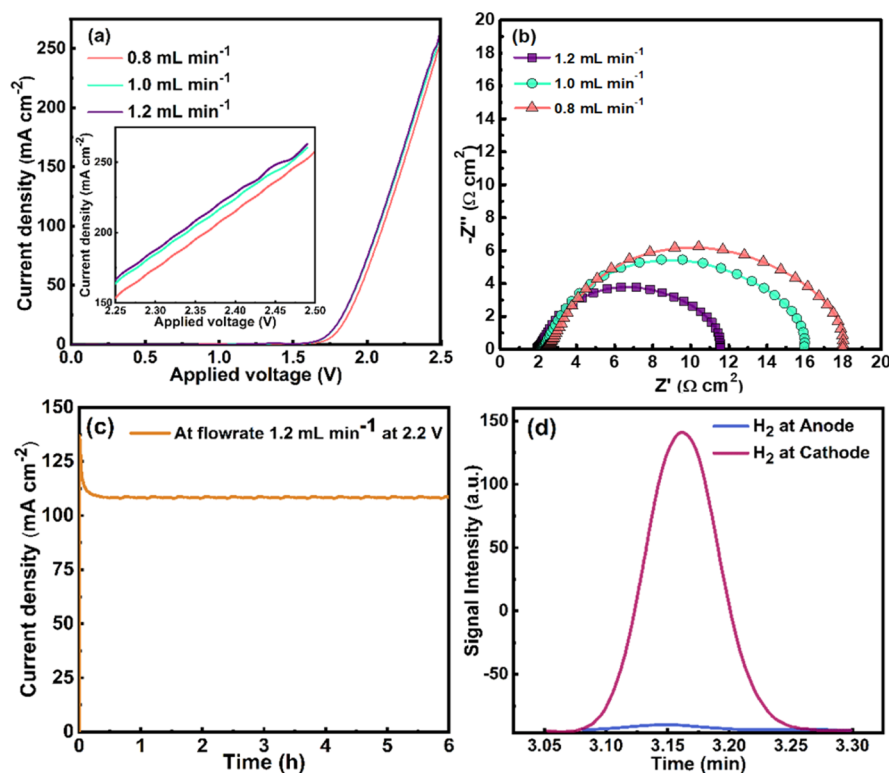


**Figure 8.** Effect of electrolyte flow rates on (a) current–voltage response; the inset depicts the current density response in the applied voltage range 2.25–2.5 V and (b) PEIS for the  $\mu$ AME with the NN15:350 catalyst. Stability analysis of the  $\mu$ AME with NN15:350 electrodes evaluated by (c) chronoamperometry and (d) gas chromatogram for product purity determination.

cm<sup>2</sup>). The losses in the  $\mu$ AME were mainly because of reaction kinetics, as the voltage loss, which accounts for ohmic resistance, was up to 18.8 mV.  $R_{ct}$ , which results from the electron transfer, was 11.56  $\Omega$  cm<sup>2</sup> for the  $\mu$ AME with NN15:350 electrodes. The  $R_{ct}$  value for the  $\mu$ AME with Pt:100 electrodes was high compared to that with NN15:350 electrodes, as can be interpreted from Figure 6b. The data were in accordance with the results obtained in the half-cell study for HER and OER activity of Pt and NN15:350 electrocatalysts.

The gas products (H<sub>2</sub> red and blue O<sub>2</sub>) evolving on the respective electrodes in the microchannel of the  $\mu$ AME are described in Figure 7a. The generated gas products were transported laterally by convection in the direction induced by electrolyte flow. An optimized electrolyte flow rate inhibits bubble intermixing and coalescence because of rapid bubble detachment from the surface of the electrode and short residence time in the microchannel. The gas products were transported to the microchannel exit and discretely collected at the downstream Y-junction.

The Segre–Silberberg effect has received enormous attention from researchers for microfluidic applications where precise control on the flow and particle is necessary, like sorting, focusing, filtering, and separation in the microchannel.<sup>57–60</sup> The Segre–Silberberg effect<sup>61–63</sup> describes the arrangement of the solid particle suspension at an off-center position in an internal laminar flow determined by the velocity. The particle trajectory is governed by the equilibrium position, which is dependent on the balance of two forces: a high-pressure force between the microchannel wall and the particle, counteracted by inertial lift force imposed by the liquid velocity gradient toward the wall across the particle's

body.<sup>61,64–66</sup> The gas cross-over in the  $\mu$ AME was averted by exploiting the Segre–Silberberg effect in the laminar flow regime. As gas bubbles are deformable, their equilibrium position can be directed further away from the wall as they experience an additional lift force. An optimized fluid flow rate can circumvent this problem by keeping the bubble far from the microchannel center.<sup>59</sup>

The still images of the gas bubbles generated by electrolysis on the NN15:350 electrode surface, maintained at a constant applied potential of 2.2 V, at some intermediate point, and the exit of the microchannel were captured (Figure 7b) under varying electrolyte flow rates (0.8–1.2 mL min<sup>-1</sup>). The images serve as a tool for visual assessment to observe the behavior and separation mechanism of the gas products, as discussed above. The bubble size decreases with an increase in the flow rate from 0.8 to 1.2 mL min<sup>-1</sup>. This is due to the large drag force experienced at the gas–liquid interface and an increased inertial lift force, which controls the separation of the H<sub>2</sub> and O<sub>2</sub> streams.<sup>67</sup> At low flow rates, the product cross-over is influenced by convective mixing of the bubbles by radial migration toward the center of the microchannel, whereas, at a high flow rate, interelectrode diffusion of the dissolved gases may cause cross-over. The same observation can be seen in the Supporting Information Movie, as the inertial lift force and the viscous drag force play an imperative role in separating H<sub>2</sub> and O<sub>2</sub>.

The current density for water electrolysis with varying electrolyte flow rates (0.8–1.2 mL min<sup>-1</sup>) was inspected by the polarization curve for the  $\mu$ AME with the NN15:350 electrocatalyst (Figure 8a). The current density increased from 258.57 mA cm<sup>-2</sup> at 0.8 mL min<sup>-1</sup> to 263.73 mA cm<sup>-2</sup> at 1.2 mL min<sup>-1</sup> at 2.5 V. A minimal change in current density

( $\sim 5.16 \text{ mA cm}^{-2}$ ) with the increasing flow rate was observed. However, the flow rate has a massive implication on product separation. The bubble nucleated on the electrode surface experiences a large drag force at a high flow rate resulting in a decrease in bubble detachment size. This minimized the mass transport resistance associated with bubbles adhering to the electrode surface, resulting in the availability of active sites for reaction.

The transition from slug flow at a low flow rate ( $0.8 \text{ mL min}^{-1}$ ) to bubble flow at a high flow rate ( $1.2 \text{ mL min}^{-1}$ ) in the microchannel, as observed in Figure 8b and the Supporting Information Movie, was interpreted relating to the change in resistances by PEIS, as shown in Figure 8b. The PEIS is sensitive to the flow behavior in the microchannel. The presence of slugs, bubbles, or a continuous phase on the electrode surface significantly changes the conductivity of ions in both phases.<sup>68</sup>  $R_{\Omega}$  attributable to the solution resistance was higher ( $2.35\text{--}2.13 \text{ } \Omega \text{ cm}^2$ ) at low flow rates ( $0.8\text{--}1.0 \text{ mL min}^{-1}$ ) owing to slug flow, which contrasts with the optimized flow rate of  $1.2 \text{ mL min}^{-1}$  ( $1.88 \text{ } \Omega \text{ cm}^2$ ) where the bubble flow was prominent. Similarly, at low flow rates ( $0.8\text{--}1.0 \text{ mL min}^{-1}$ ),  $R_{ct}$  is higher ( $18\text{--}15.98 \text{ } \Omega \text{ cm}^2$ ) in comparison to that at a high flow rate ( $1.2 \text{ mL min}^{-1}$ ,  $11.56 \text{ } \Omega \text{ cm}^2$ ). This is caused by the presence of a large gas volume fraction at a low flow rate. At a high flow rate, the interfacial area of the bubble increases because of the transition from the slug to bubble flow in the microchannel.

The viscous laminar flow and the convective gas product transport in the microchannel were characterized by dimensionless number analysis (Table S1). The Reynolds number was estimated to be in the range of  $25.10\text{--}37.33$  for the electrolyte flow rate of  $0.8\text{--}1.2 \text{ mL min}^{-1}$  in the  $\mu\text{AME}$ . The low Reynolds number implies the dominance of viscous flow in the microchannel, thereby inhibiting the mixing of  $\text{H}_2$  and  $\text{O}_2$  and prevent cross-over. However, there is a possibility of gas products dissolving in a minimal amount and diffusing across the channel width, causing gas impurities. To evade this, a high Peclet number is desirable for the convenient transport of the dissolved gases through the microchannel. The Peclet number for the electrolyzer operating at  $1.2 \text{ mL min}^{-1}$  was evaluated based on the diffusivity of  $\text{H}_2$  and  $\text{O}_2$  to be  $6.25 \times 10^3$  and  $1.5 \times 10^4$ , respectively. This suggests the appropriate functioning of the  $\mu\text{AME}$  to produce pure fuel due to negligible gas product diffusion across the electrodes.

Chronoamperometry (CA) was performed under a constant applied potential of  $2.2 \text{ V}$  to investigate the resilience of the  $\mu\text{AME}$  with the bifunctional NN15:350 electrocatalyst for the continuous  $\text{H}_2$  and  $\text{O}_2$  production (Figure 8c). The device operating at  $1.2 \text{ mL min}^{-1}$  exhibits stable operation for  $6 \text{ h}$  with no significant variation in current density. The convective gas product transport along the length of the  $\mu\text{AME}$  diminishes the gas cross-over, which results in a constant ionic resistance between the electrodes. The gases at the exit of the Y-channel were collected to analyze the purity by gas chromatography. Figure 8d shows the chromatogram of  $\text{H}_2$  at the cathode and anode. The  $\text{H}_2$  obtained at the anode corresponds to product cross-over, which was negligible, as shown in the Supporting Information Movie and Figure 8b. The  $\text{H}_2$  obtained at the cathode is suitable for use as a fuel, and the  $\mu\text{AME}$  demonstrates safe operation without membranes. Moreover, the volumetric collection efficiencies (refer to Supporting Information) of  $\text{H}_2$  and  $\text{O}_2$  were  $97.72$  and  $96.14\%$ ,

respectively, indicating minimum gas dissolution in the gas-tight electrolyte connection of tube fittings and ports.

A critical parameter for consideration in the design of the  $\mu\text{AME}$  is selecting an optimum interelectrode distance. In a membrane-based electrolyzer, a thin MEA is required for a low ionic resistance between the anode and cathode, while facilitating ion migration.<sup>69</sup> In the  $\mu\text{AME}$ , the interelectrode distance interplays between the fluidic and ionic resistances. The likelihood of gas product intermixing increases in the microchannel with a small interelectrode distance.

A small interelectrode distance will increase the likelihood of gas product mixing, leading to the deviation from laminar flow. A high ohmic resistance will be exerted by a sizeable interelectrode distance because of the significant path length for ion transfer across the electrode. To rationalize the interelectrode distance used in the present study, we calculate the maximum energy conversion efficiency, which compares the energy stored in the product to the power loss from fluidic and ionic resistances as a function of interelectrode distance.<sup>70</sup> The energy conversion efficiency for the  $\mu\text{AME}$  for overall water splitting was estimated to be  $99.86\%$  (detailed calculation made in Supporting Information), which substantiates the  $150 \text{ } \mu\text{m}$  interelectrode distance.

The energy density of  $\text{H}_2$  generated in the  $\mu\text{AME}$  can suffice the electrolyte pumping power requirement. The pumping power accounts for only  $5\%$  of the energy stored in  $\text{H}_2$  produced by water electrolysis in the membraneless microfluidic electrolyzer.<sup>16,71</sup> A low pumping power and a high energy density product from the  $\mu\text{AME}$  serve as an impetus for commercial scale-up of the miniaturized technology. The  $\mu\text{AME}$  can be scaled up by manifold parallelized arrangement due to the low pumping power.

Identifying the length scale of the transport processes required in the micron scale is imperative to the scale-up of the  $\mu\text{AME}$ . The electrode area can be scaled to a macroscale with the microscale interelectrode distance if the parallelization occurs in an orthogonal direction to the electrolyte flow. This will enable multiple microchannels for water electrolysis to be stacked to accommodate multiple electrolyzers into a single unit to attain a high  $\text{H}_2$  throughput.

The fabrication technique of the scaled-up  $\mu\text{AME}$  system will govern the manufacturability and cost of the final product. A new paradigm is introduced by the advances in 3D micro additive manufacturing, enabling the fabrication of personalized prototypes to meet the desired  $\text{H}_2$  demand.<sup>17,72</sup> This will pave the way for the scale-up of the microfluidic electrolyzer with a high  $\text{H}_2$  throughput to compete with the membrane-based counterparts.

#### 4. CONCLUSIONS

A bifunctional  $\text{Ni}_3\text{N}/\text{Ni}$  microelectrode was developed using  $\text{NH}_3$  plasma for overall water electrolysis in microfluidic devices. The bifunctional catalyst exhibited better performance than a Pt thin film catalyst, which is widely used in microfabrication. The enhanced performance of the  $\text{Ni}_3\text{N}/\text{Ni}$  under optimized conditions is attributable to the presence of surface-confined N–H moieties and close contact of the  $\text{Ni}_3\text{N}$ –Ni interface induced by  $\text{NH}_3$  plasma. The methodology for the catalyst synthesis is scalable and compatible with the microfabrication process for microfluidic device fabrication. A membraneless microfluidic reactor was fabricated by the soft lithography and lift-off technique, incorporating the bifunctional  $\text{Ni}_3\text{N}/\text{Ni}$  catalyst. A qualitative visualization tool was

used to analyze the flow of gas-electrolyte in the microchannel and provided insights into the effect of the flow rate, which is the interplay between the viscous force and lift force. The membraneless electrolyzer exhibited a continuous stable operation with no gas cross-over across the electrode characterized by gas chromatography. The facile operation of the microfluidic electrolyzer will surpass the performance of a membrane-based electrolyzer operating under stringent conditions, thus paving the way in research for scale-up and gas product storage.

## ■ ASSOCIATED CONTENT

### SI Supporting Information

The Supporting Information is available free of charge at <https://pubs.acs.org/doi/10.1021/acsaem.1c01772>.

Dimensionless number analysis, comparison of HER activity of the NN15:350 catalyst with other non-noble electrocatalysts in the alkaline electrolyte, comparison of OER activity of the NN15:350 catalyst with other non-noble electrocatalysts in the alkaline electrolyte, volumetric H<sub>2</sub> and O<sub>2</sub> collection efficiency, and interelectrode distance-based energy conversion efficiency (PDF)

Qualitative flow visualization of the two-phase flow in the microchannel (AVI)

## ■ AUTHOR INFORMATION

### Corresponding Authors

Anastasia Elias – Donadeo Innovation Centre for Engineering, Department of Chemical and Materials Engineering, University of Alberta, Edmonton, Alberta T6G 1H9, Canada; [orcid.org/0000-0002-6737-0271](https://orcid.org/0000-0002-6737-0271); Email: [aelias@ualberta.ca](mailto:aelias@ualberta.ca)

Suddhasatwa Basu – Department of Chemical Engineering, Indian Institute of Technology Delhi Hauz Khas, New Delhi 110016, India; [orcid.org/0000-0001-7288-2370](https://orcid.org/0000-0001-7288-2370); Email: [sbasu@chemical.iitd.ac.in](mailto:sbasu@chemical.iitd.ac.in)

### Authors

Biswajit S. De – Department of Chemical Engineering, Indian Institute of Technology Delhi Hauz Khas, New Delhi 110016, India

Pawan Kumar – Department of Chemical and Petroleum Engineering, University of Calgary, Calgary, Alberta T2N 1N4, Canada

Neeraj Khare – Department of Physics, Indian Institute of Technology Delhi Hauz Khas, New Delhi 110016, India; [orcid.org/0000-0003-3702-2257](https://orcid.org/0000-0003-3702-2257)

Jing-Li Luo – Donadeo Innovation Centre for Engineering, Department of Chemical and Materials Engineering, University of Alberta, Edmonton, Alberta T6G 1H9, Canada; [orcid.org/0000-0002-2465-7280](https://orcid.org/0000-0002-2465-7280)

Complete contact information is available at: <https://pubs.acs.org/doi/10.1021/acsaem.1c01772>

### Author Contributions

B.S.D.: Conceptualization, data curation, formal analysis, investigation, validation, visualization, and writing—original draft. P.K.: Formal analysis, visualization, and writing—review and editing. N.K.: writing—review and editing and validation. J.-L.L.: Resources and writing—review and editing. A.E.: Funding acquisition, validation, writing—review and editing,

resources, and supervision. S.B.: Funding acquisition, validation, writing—review and editing, resources, and supervision.

### Notes

The authors declare no competing financial interest.

## ■ ACKNOWLEDGMENTS

B.S.D. thanks SERB for the OVDF fellowship to carry out a part of his doctoral research at the University of Alberta, Canada. Samples were fabricated and characterized at the University of Alberta Nanofab. Support from the Natural Sciences and Engineering Research Council of Canada is gratefully acknowledged.

## ■ REFERENCES

- (1) Kumar, P.; Kar, P.; Manuel, A. P.; Zeng, S.; Thakur, U. K.; Alam, K. M.; Zhang, Y.; Kisslinger, R.; Cui, K.; Bernard, G. M.; Michaelis, V. K.; Shankar, K. Noble Metal Free, Visible Light Driven Photocatalysis Using TiO<sub>2</sub> Nanotube Arrays Sensitized by P-Doped C<sub>3</sub>N<sub>4</sub> Quantum Dots. *Adv. Opt. Mater.* **2020**, *8*, 1901275–1901289.
- (2) Nocera, D. G. Chemistry of Personalized Solar Energy. *Inorg. Chem.* **2009**, *48*, 10001–10017.
- (3) Chavhan, M. P.; Basu, D.; Singh, A.; Ganguly, S. N-Doping in Precursor Sol: Some Observations in Reference to In Situ-Grown Carbon Film Electrodes for Supercapacitor Applications. *Energy Technol.* **2020**, *8*, 1901479.
- (4) Navarro-Flores, E.; Chong, Z.; Omanovic, S. Characterization of Ni, NiMo, NiW and NiFe Electroactive Coatings as Electrocatalysts for Hydrogen Evolution in an Acidic Medium. *J. Mol. Catal. A Chem.* **2005**, *226*, 179–197.
- (5) McCrory, C. C. L.; Jung, S.; Peters, J. C.; Jaramillo, T. F. Benchmarking Heterogeneous Electrocatalysts for the Oxygen Evolution Reaction. *J. Am. Chem. Soc.* **2013**, *135*, 16977–16987.
- (6) Jang, S.; Kim, M.; Kang, Y. S.; Choi, Y. W.; Kim, S. M.; Sung, Y.-E.; Choi, M. Facile Multiscale Patterning by Creep-Assisted Sequential Imprinting and Fuel Cell Application. *ACS Appl. Mater. Interfaces* **2016**, *8*, 11459–11465.
- (7) Faunce, T. A.; Lubitz, W.; Rutherford, A. W.; MacFarlane, D.; Moore, G. F.; Yang, P.; Nocera, D. G.; Moore, T. A.; Gregory, D. H.; Fukuzumi, S.; Yoon, K. B.; Armstrong, F. A.; Wasielewski, M. R.; Styring, S. Energy and Environment Policy Case for a Global Project on Artificial Photosynthesis. *Energy Environ. Sci.* **2013**, *6*, 695–698.
- (8) Singh, A.; Tejasvi, R.; Karmakar, S.; Basu, S.  $\alpha$ -Fe<sub>2</sub>O<sub>3</sub> Nanorods Decorated with NiMnO<sub>3</sub> Co-Catalyst as Photoanode for Enhanced Oxygen Evolution Reaction in Photoelectrochemical Water Splitting. *Mater. Today Commun.* **2021**, *27*, 102231.
- (9) Singh, A.; Sarma, S. K.; Karmakar, S.; Basu, S. Photocatalytic H<sub>2</sub>O<sub>2</sub> Generation Assisted Photoelectrochemical Water Oxidation for Enhanced BiVO<sub>4</sub> Photoanode Performance. *Chem. Eng. J. Adv.* **2021**, *8*, 100142.
- (10) Xu, W.; Scott, K.; Basu, S. Performance of a High Temperature Polymer Electrolyte Membrane Water Electrolyser. *J. Power Sources* **2011**, *196*, 8918–8924.
- (11) Epting, W. K.; Gelb, J.; Litster, S. Resolving the Three-Dimensional Microstructure of Polymer Electrolyte Fuel Cell Electrodes Using Nanometer-Scale X-ray Computed Tomography. *Adv. Funct. Mater.* **2012**, *22*, 555–560.
- (12) Saha, S.; Gayen, P.; Wang, Z.; Dixit, R. J.; Sharma, K.; Basu, S.; Ramani, V. K. Development of Bimetallic PdNi Electrocatalysts toward Mitigation of Catalyst Poisoning in Direct Borohydride Fuel Cells. *ACS Catal.* **2021**, *11*, 8417–8430.
- (13) Guima, K.-E.; Gomes, L. E.; Alves Fernandes, J.; Wender, H.; Martins, C. A. Harvesting Energy from an Organic Pollutant Model Using a New 3D-Printed Microfluidic Photo Fuel Cell. *ACS Appl. Mater. Interfaces* **2020**, *12*, 54563–54572.
- (14) De, B. S.; Singh, A.; Elias, A.; Khare, N.; Basu, S. An Electrochemical Neutralization Energy-Assisted Membrane-Less

Microfluidic Reactor for Water Electrolysis. *Sustain. Energy Fuels* **2020**, *4*, 6234–6244.

(15) Ortiz-Ortega, E.; Díaz-Patiño, L.; Bejar, J.; Trejo, G.; Guerra-Balcázar, M.; Espinosa-Magaña, F.; Álvarez-Contreras, L.; Arriaga, L. G.; Arjona, N. A Flow-Through Membraneless Microfluidic Zinc-Air Cell. *ACS Appl. Mater. Interfaces* **2020**, *12*, 41185–41199.

(16) Hashemi, S. M. H.; Psaltis, D.; Psaltis, D. A Membrane-Less Electrolyzer for Hydrogen Production across the PH Scale. *Energy Environ. Sci.* **2015**, *8*, 2003–2009.

(17) Hashemi, S. M. H.; Hadikhani, P.; Chinello, E.; Litvinov, S.; Moser, C.; Koumoutsakos, P.; Psaltis, D.; Psaltis, D. A Versatile and Membrane-Less Electrochemical Reactor for the Electrolysis of Water and Brine. *Energy Environ. Sci.* **2019**, *12*, 1592–1604.

(18) Ayers, K. E.; Renner, J. N.; Danilovic, N.; Wang, J. X.; Zhang, Y.; Maric, R.; Yu, H. Pathways to Ultra-Low Platinum Group Metal Catalyst Loading in Proton Exchange Membrane Electrolyzers. *Catal. Today* **2016**, *262*, 121–128.

(19) Oruc, M. E.; Desai, A. V.; Nuzzo, R. G.; Kenis, P. J. A. Design, Fabrication, and Characterization of a Proposed Microchannel Water Electrolyzer. *J. Power Sources* **2016**, *307*, 122–128.

(20) Han, N.; Luo, S.; Deng, C.; Zhu, S.; Xu, Q.; Min, Y. Defect-Rich Fe<sub>0.023</sub>/Mo<sub>2</sub>C Heterostructure as a Highly Efficient Bifunctional Catalyst for Overall Water-Splitting. *ACS Appl. Mater. Interfaces* **2021**, *13*, 8306–8314.

(21) Wei, Y.; Zou, P.; Yue, Y.; Wang, M.; Fu, W.; Si, S.; Wei, L.; Zhao, X.; Hu, G.; Xin, H. L. One-Pot Synthesis of B/P-Codoped Co-Mo Dual-Nanowafers Electrochemicals for Overall Water Splitting. *ACS Appl. Mater. Interfaces* **2021**, *13*, 20024–20033.

(22) Zang, Z.; Wang, X.; Li, X.; Zhao, Q.; Li, L.; Yang, X.; Yu, X.; Zhang, X.; Lu, Z. Co<sub>9</sub>S<sub>8</sub> Nanosheet Coupled Cu<sub>2</sub>S Nanorod Heterostructure as Efficient Catalyst for Overall Water Splitting. *ACS Appl. Mater. Interfaces* **2021**, *13*, 9865–9874.

(23) Ouyang, B.; Zhang, Y.; Zhang, Z.; Fan, H. J.; Rawat, R. S. Nitrogen-Plasma-Activated Hierarchical Nickel Nitride Nanocorals for Energy Applications. *Small* **2017**, *13*, 1604265.

(24) Liu, B.; He, B.; Peng, H. Q.; Zhao, Y.; Cheng, J.; Xia, J.; Shen, J.; Ng, T. W.; Meng, X.; Lee, C. S.; Zhang, W. Unconventional Nickel Nitride Enriched with Nitrogen Vacancies as a High-Efficiency Electrocatalyst for Hydrogen Evolution. *Adv. Sci.* **2018**, *5*, 1800406.

(25) Zhang, Y.; Ouyang, B.; Xu, J.; Chen, S.; Rawat, R. S.; Fan, H. J. 3D Porous Hierarchical Nickel–Molybdenum Nitrides Synthesized by RF Plasma as Highly Active and Stable Hydrogen-Evolution-Reaction Electrocatalysts. *Adv. Energy Mater.* **2016**, *6*, 1600221.

(26) Yan, Y.; Cheng, X.; Zhang, W.; Chen, G.; Li, H.; Konkin, A.; Sun, Z.; Sun, S.; Wang, D.; Schaaf, P. Plasma Hydrogenated TiO<sub>2</sub>/Nickel Foam as an Efficient Bifunctional Electrocatalyst for Overall Water Splitting. *ACS Sustain. Chem. Eng.* **2019**, *7*, 885–894.

(27) Jin, Q.; Ren, B.; Li, D.; Cui, H.; Wang, C. Plasma-Assisted Synthesis of Self-Supporting Porous CoNPs@C Nanosheet as Efficient and Stable Bifunctional Electrocatalysts for Overall Water Splitting. *ACS Appl. Mater. Interfaces* **2017**, *9*, 31913–31921.

(28) Wang, H.; Xiong, J.; Cheng, X.; Fritz, M.; Ispas, A.; Bund, A.; Chen, G.; Wang, D.; Schaaf, P. Ni<sub>3</sub>N-Coated Ni Nanorod Arrays for Hydrogen and Oxygen Evolution in Electrochemical Water Splitting. *ACS Appl. Nano Mater.* **2020**, *3*, 10986–10995.

(29) Chen, T.; Zhang, R.; Chen, G.; Huang, J.; Chen, W.; Wang, X.; Chen, D.; Li, C.; Ostrikov, K. Plasma-Doping-Enhanced Overall Water Splitting: Case Study of NiCo Hydroxide Electrocatalyst. *Catal. Today* **2019**, *337*, 147–154.

(30) He, L.; Zhou, D.; Lin, Y.; Ge, R.; Hou, X.; Sun, X.; Zheng, C. Ultrarapid In Situ Synthesis of Cu<sub>2</sub>S Nanosheet Arrays on Copper Foam with Room-Temperature-Active Iodine Plasma for Efficient and Cost-Effective Oxygen Evolution. *ACS Catal.* **2018**, *8*, 3859–3864.

(31) Kumar, P.; Singh, M.; Reddy, G. B. Core-Shell WO<sub>3</sub>-WS<sub>2</sub> Nanostructured Thin Films via Plasma Assisted Sublimation and Sulfurization. *ACS Appl. Nano Mater.* **2019**, *2*, 1691–1703.

(32) Li, G.; Wu, X.; Guo, H.; Guo, Y.; Chen, H.; Wu, Y.; Zheng, J.; Li, X. Plasma Transforming Ni(OH)<sub>2</sub> Nanosheets into Porous Nickel

Nitride Sheets for Alkaline Hydrogen Evolution. *ACS Appl. Mater. Interfaces* **2020**, *12*, 5951–5957.

(33) Chen, H.; Zhao, Q.; Gao, L.; Ran, J.; Hou, Y. Water-Plasma Assisted Synthesis of Oxygen-Enriched Ni-Fe Layered Double Hydroxide Nanosheets for Efficient Oxygen Evolution Reaction. *ACS Sustain. Chem. Eng.* **2019**, *7*, 4247–4254.

(34) Liang, H.; Gandi, A. N.; Anjum, D. H.; Wang, X.; Schwingenschlögl, U.; Alshareef, H. N. Plasma-Assisted Synthesis of NiCoP for Efficient Overall Water Splitting. *Nano Lett.* **2016**, *16*, 7718–7725.

(35) Aaltonen, T.; Ritala, M.; Sajavaara, T.; Keinonen, J.; Leskelä, M. Atomic Layer Deposition of Platinum Thin Films. *Chem. Mater.* **2003**, *15*, 1924–1928.

(36) Dixit, R. J.; Bhattacharyya, K.; Ramani, V. K.; Basu, S. Electrocatalytic Hydrogenation of Furfural Using Non-Noble-Metal Electrocatalysts in Alkaline Medium. *Green Chem.* **2021**, *23*, 4201–4212.

(37) Kreider, M. E.; Gallo, A.; Back, S.; Liu, Y.; Siahrostami, S.; Nordlund, D.; Sinclair, R.; Nørskov, J. K.; King, L. A.; Jaramillo, T. F. Precious Metal-Free Nickel Nitride Catalyst for the Oxygen Reduction Reaction. *ACS Appl. Mater. Interfaces* **2019**, *11*, 26863–26871.

(38) Lucentini, I.; Casanovas, A.; Llorca, J. Catalytic Ammonia Decomposition for Hydrogen Production on Ni, Ru and Ni[Sbnd]Ru Supported on CeO<sub>2</sub>. *Int. J. Hydrogen Energy* **2019**, *44*, 12693–12707.

(39) Mukherjee, S.; Devaguptapu, S. V.; Sviripa, A.; Lund, C. R. F.; Wu, G. Low-Temperature Ammonia Decomposition Catalysts for Hydrogen Generation. *Appl. Catal. B Environ.* **2018**, *226*, 162–181.

(40) Mebrahtu, C.; Abate, S.; Perathoner, S.; Chen, S.; Centi, G. CO<sub>2</sub> Methanation over Ni Catalysts Based on Ternary and Quaternary Mixed Oxide: A Comparison and Analysis of the Structure-Activity Relationships. *Catal. Today* **2018**, *304*, 181–189.

(41) Grosvenor, A. P.; Biesinger, M. C.; Smart, R. S. C.; McIntyre, N. S. New Interpretations of XPS Spectra of Nickel Metal and Oxides. *Surf. Sci.* **2006**, *600*, 1771–1779.

(42) Zhang, N.; Zou, Y.; Tao, L.; Chen, W.; Zhou, L.; Liu, Z.; Zhou, B.; Huang, G.; Lin, H.; Wang, S. Electrochemical Oxidation of 5-Hydroxymethylfurfural on Nickel Nitride/Carbon Nanosheets: Reaction Pathway Determined by In Situ Sum Frequency Generation Vibrational Spectroscopy. *Angew. Chem.* **2019**, *131*, 16042–16050.

(43) Feng, X.; Wang, H.; Bo, X.; Guo, L. Bimetal-Organic Framework-Derived Porous Rodlike Cobalt/Nickel Nitride for All-PH Value Electrochemical Hydrogen Evolution. *ACS Appl. Mater. Interfaces* **2019**, *11*, 8018–8024.

(44) Song, F.; Li, W.; Yang, J.; Han, G.; Liao, P.; Sun, Y. Interfacial Nickel Nitride and Nickel Boosts Both Electrocatalytic Hydrogen Evolution and Oxidation Reactions. *Nat. Commun.* **2018**, *9*, 4531–4541.

(45) Wang, Z.; Xu, L.; Huang, F.; Qu, L.; Li, J.; Owusu, K. A.; Liu, Z.; Lin, Z.; Xiang, B.; Liu, X.; Zhao, K.; Liao, X.; Yang, W.; Cheng, Y. B.; Mai, L. Copper–Nickel Nitride Nanosheets as Efficient Bifunctional Catalysts for Hydrazine-Assisted Electrolytic Hydrogen Production. *Adv. Energy Mater.* **2019**, *9*, 1900390.

(46) Saad, A.; Cheng, Z.; Zhang, X.; Liu, S.; Shen, H.; Thomas, T.; Wang, J.; Yang, M. Ordered Mesoporous Cobalt–Nickel Nitride Prepared by Nanocasting for Oxygen Evolution Reaction Electro-catalysis. *Adv. Mater. Interfaces* **2019**, *6*, 1900960.

(47) Hu, C.; Zhang, L.; Gong, J. Recent Progress Made in the Mechanism Comprehension and Design of Electrocatalysts for Alkaline Water Splitting. *Energy Environ. Sci.* **2019**, *12*, 2620–2645.

(48) Bockris, J. O. M. Kinetics of Activation Controlled Consecutive Electrochemical Reactions: Anodic Evolution of Oxygen. *J. Chem. Phys.* **1956**, *24*, 817–827.

(49) Edwards, T. C.; Steer, M. B. *Foundations for Microstrip Circuit Design*; John Wiley & Sons, 2016.

(50) Bakonyi, I.; Isnaini, V. A.; Kolonits, T.; Czigány, Z.; Gubicza, J.; Varga, L. K.; Tóth-Kádár, E.; Pogány, L.; Péter, L.; Ebert, H. The Specific Grain-Boundary Electrical Resistivity of Ni. *Philos. Mag.* **2019**, *99*, 1139–1162.

- (51) Aihaiti, L.; Tuokedaerhan, K.; Sadeh, B.; Zhang, M.; Shen, X.; Mijiti, A. Effect of Annealing Temperature on Microstructure and Resistivity of TiC Thin Films. *Coatings* **2021**, *11*, 457–470.
- (52) Xu, K.; Chen, P.; Li, X.; Tong, Y.; Ding, H.; Wu, X.; Chu, W.; Peng, Z.; Wu, C.; Xie, Y. Metallic Nickel Nitride Nanosheets Realizing Enhanced Electrochemical Water Oxidation. *J. Am. Chem. Soc.* **2015**, *137*, 4119–4125.
- (53) Diard, J.-P.; LeGorrec, B.; Maximovitch, S. Etude de l'activation Du Degagement d'hydrogene Sur Electrode d'oxyde de Nickel Par Spectroscopie d'impedance. *Electrochim. Acta* **1990**, *35*, 1099–1108.
- (54) Vermaas, D. A.; Wiegman, S.; Nagaki, T.; Smith, W. A. Ion Transport Mechanisms in Bipolar Membranes for (Photo) Electrochemical Water Splitting. *Sustain. Energy Fuels* **2018**, *2*, 2006–2015.
- (55) Vermaas, D. A.; Sassenburg, M.; Smith, W. A. Photo-Assisted Water Splitting with Bipolar Membrane Induced PH Gradients for Practical Solar Fuel Devices. *Angew. Chem.* **2015**, *3*, 19556–19562.
- (56) Xiang, C.; Papadantonakis, K. M.; Lewis, N. S. Principles and Implementations of Electrolysis Systems for Water Splitting. *Mater. Horiz.* **2016**, *3*, 169–173.
- (57) Bhagat, A. A. S.; Kuntaegowdanahalli, S. S.; Papautsky, I. Enhanced Particle Filtration in Straight Microchannels Using Shear-Modulated Inertial Migration. *Phys. Fluids* **2008**, *20*, 101702.
- (58) Kuntaegowdanahalli, S. S.; Bhagat, A. A. S.; Kumar, G.; Papautsky, I. Inertial Microfluidics for Continuous Particle Separation in Spiral Microchannels. *Lab Chip* **2009**, *9*, 2973–2980.
- (59) Amini, H.; Lee, W.; Di Carlo, D. Inertial Microfluidic Physics. *Lab Chip* **2014**, *14*, 2739–2761.
- (60) Di Carlo, D. Inertial Microfluidics. *Lab Chip* **2009**, *9*, 3038–3046.
- (61) Segré, G.; Silberberg, A. Radial Particle Displacements in Poiseuille Flow of Suspensions. *Nature* **1961**, *189*, 209.
- (62) Segré, G.; Silberberg, A. Behaviour of Macroscopic Rigid Spheres in Poiseuille Flow Part 1. Determination of Local Concentration by Statistical Analysis of Particle Passages through Crossed Light Beams. *J. Fluid Mech.* **1962**, *14*, 115–135.
- (63) Segré, G.; Silberberg, A. Behaviour of Macroscopic Rigid Spheres in Poiseuille Flow Part 2. Experimental Results and Interpretation. *J. Fluid Mech.* **1962**, *14*, 136–157.
- (64) Schonberg, J. A.; Hinch, E. J. Inertial Migration of a Sphere in Poiseuille Flow. *J. Fluid Mech.* **1989**, *203*, 517–524.
- (65) McLaughlin, J. B. The Lift on a Small Sphere in Wall-Bounded Linear Shear Flows. *J. Fluid Mech.* **1993**, *246*, 249–265.
- (66) McLaughlin, J. B. Inertial Migration of a Small Sphere in Linear Shear Flows. *J. Fluid Mech.* **1991**, *224*, 261–274.
- (67) Basu, S.; Nandakumar, K.; Masliyah, J. H. A Study of Oil Displacement on Model Surfaces. *J. Colloid Interface Sci.* **1996**, *182*, 82–94.
- (68) Polezhaev, P.; Slouka, Z.; Lindner, J.; Přibyl, M. Characterization of Slug Flow of Two Aqueous Phases by Electrochemical Impedance Spectroscopy in a Fluidic Chip. *Microelectron. Eng.* **2018**, *194*, 89–95.
- (69) Ayers, K. E.; Anderson, E. B.; Capuano, C.; Carter, B.; Dalton, L.; Hanlon, G.; Manco, J.; Niedzwiecki, M. Research Advances towards Low Cost, High Efficiency PEM Electrolysis. *ECS Trans.* **2010**, *33*, 3–15.
- (70) Modestino, M. A.; Fernandez Rivas, D.; Hashemi, S. M. H.; Gardeniers, J. G. E.; Psaltis, D. The Potential for Microfluidics in Electrochemical Energy Systems. *Energy Environ. Sci.* **2016**, *9*, 3381–3391.
- (71) Pang, X.; Davis, J. T.; Harvey, A. D.; Esposito, D. V. Framework for Evaluating the Performance Limits of Membraneless Electrolyzers. *Energy Environ. Sci.* **2020**, *13*, 3663–3678.
- (72) Bui, J. C.; Davis, J. T.; Esposito, D. V. 3D-Printed Electrodes for Membraneless Water Electrolysis. *Sustain. Energy Fuels* **2019**, *4*, 213–225.